General Disclaimer

One or more of the Following Statements may affect this Document

NASA CR-165265

R81AEG215

NASA

National Aeronautics and
Space Administration

ANALYSIS, DESIGN, FABRICATION AND TESTING OF AN OPTICAL TIP CLEARANCE SENSOR

FINAL REPORT
May 1981

by

G.L. Poppel, D.T.F. Marple, and J.D. Kingsley
A.R. Mulukutla, Program Manager

General Electric Company
Aircraft Engine Business Group
Advanced Engineering and Technology Programs Department
Cincinnati, Ohio 45215
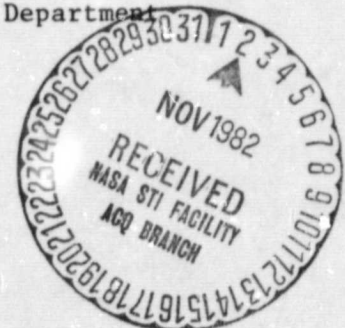
Prepared For
R.J. Baumbick, Project Manager

National Aeronautics and Space Administration

NASA-Lewis Research Center
21000 Brookpark Road
Cleveland, Ohio 44135

Contract No. NAS3-21843

1. Report No. CR-165265	2. Government Accession No.	3. Recipient's Catalog No
4. Title and Subtitle Analysis, Design, Fabrication and Testing of an Optical Tip Clearance Sensor		5. Report Date May 1981
		6. Performing Organization Code Class II
7. Author(s) G.L. Poppel, D.T.F. Marple, C.D. Kingsley		8. Performing Organization Report No R81AEG215
		10. Work Unit No
9. Performing Organization Name and Address General Electric Company Aircraft Engine Business Group 1 Neumann Way Evendale, Ohio 45215		
		11. Contract or Grant No NAS3-21843
		13. Type of Report and Period Covered (June 79 - Jan. 81 (Contract Report)
12. Sponsoring Agency Name and Address NASA-Lewis Research Center 21000 Brookpark Road Cleveland, Ohio 44135		
		14. Sponsoring Agency Code

15. Supplementary Notes

16. Abstract

The objective of the program reported here was to perform analyses and carry out the design, fabrication, and testing of an optical tip clearance sensor with intended application in aircraft propulsion control systems. This concept arose as a result of a study carried out under a previous NASA program, Contract NAS3-21006. The report discusses the design of a sensor test rig, evaluation of optical sensor components at elevated temperatures, sensor design principles, sensor test results at room temperature, and estimations of sensor accuracy at temperatures of an aircraft engine environment. Room temperature testing indicated possible measurement accuracies of less than 12.7 µm (0.5 mils). Recommendations are presented of ways to improve performance at engine operating temperatures and an assessment is given of the potential of this tip clearance sensor.

17. Key Words (Suggested by Author(s)) Tip Clearance Sensor Optical Sensor	18. Distribution Statement Unclassified: Unlimited		
19. Security Classif. (of this report) Unclassified	20. Security Classif. (of this page) Unclassified	21. No. of Pages 76	22. Price*

* For sale by the National Technical Information Service, Springfield, Virginia 22161

NASA-C-168 (Rev. 10-75)

Trade names or manufacturer's names are used in this report for
identification only. This usage does not constitute an official
endorsement, either expressed or implied, by the National
Aeronautics and Space Administration.

FOREWORD

TABLE OF CONTENTS

PRECEDING PAGE BLANK NOT FILMED

TABLE OF CONTENTS (Concluded)

LIST OF ILLUSTRATIONS

1.0 SUMMARY

The objective of this program was to perform analysis and carry out the design, fabrication and testing of an optical tip clearance sensor. The intended application for this sensor is in electronic propulsion control systems for commercial and military aircraft. The program was divided into three specific work tasks as described below:

Task I consisted of the design of a compressor rotor test rig for use in subsequent sensor concept testing, a thermal evaluation of candidate optical sensor components, and the preparation of a proposed sensor concept test plan.

Task II consisted of the fabrication, assembly, check out and balance of the test rig designed under Task I.

Task III consisted of an exploratory testing study of the selected optical tip clearance sensor concept, making use of the fabricated test rig and following the prepared sensor test plan.

After developing general design criteria for the optical tip clearance sensor concept, a sensor was designed and assembled for testing on the fabricated test rig. Testing at room temperature showed a capability of measuring blade tip clearance to an accuracy of less than 12.7 μm (0.5 mils). Estimation of sensor performance at engine operating temperatures, based on sensor component thermal evaluation results, showed a decrease in accuracy, due to a decrease in signal to noise ratio. Methods to achieve improved accuracy and a more compact design are suggested. The results of this program indicate this concept has merit for use as a control system sensor. A follow-on contract for development of an aircraft engine prototype is recommended.

2.0 INTRODUCTION

When airfoil tip clearance is excessive, aircraft gas turbine performance and efficiency are reduced. The General Electric Company has been working to decrease this loss on future commercial engines. The NASA Energy Efficient Engine, for example, is slated to use active tip clearance control on the compressor and both turbines, by using an open-loop approach to vary casing or shroud cooling air. A tip clearance sensor would allow closed-loop control which is highly preferred.

Optical sensing methods are a promising trend in sensor technology. Unlike conventional measurement methods, optical devices are noncontacting and do not require servo pressure. Optical systems thus have inherent accuracy and low weight. These properties plus a high data transmission rate permit redundant installations to ensure reliability, as could be done with fiber optic cable. Moreover, optics are highly resistant to electromagnetic interference. All of these advantages would be found on an optical tip clearance sensor, which is seen as the best potential solution to tip clearance measurement.

In 1978, at the General Electric Evendale facility, a preliminary design and analysis study (NASA CR-159434) of an optical tip clearance sensor concept was completed. The concept involved transmission of an optical signal tangentially across the rotor tip area. Performance predictions showed that application to propulsion control system is feasible and lab experiment results encouraged further development. This present program was initiated to achieve a working laboratory breadboard model of the sensor, and to evaluate its performance at engine operating temperatures.

2

3.0 SENSOR TEST RIG

3.1 TEST RIG DESIGN

3.1.1 General Description

The test rig (Figure 1), including drive motor, is mounted on a 2.54 cm (1 inch) thick aluminum base and housed on its four sides by aluminum plate material. All sides are bolted to the base and pinned with spring-dowels for accurate positioning. The base plate contains extension lugs to give the box enhanced stability and for bolting to a heavier surface. The rotor shaft is mounted through a flanged bearing housing which bolts to one of the 1.905 cm (0.75 inch) thick sides. This housing contains two grease-packed 20 mm precision ball bearings, spaced about 7.7 cm apart. The bearing inner races are clamped; the outer races are spring loaded apart to obtain a wider wheel base and eliminate play.

The test rig rotor consists of a precision ground shaft with wrench flats to facilitate torquing the bearing nuts. A TF34 Stage 9 compressor disk is bolted between two symmetrical disk clamps which are keyed to the shaft. The disk clamps also serve as baffles to help prevent airflow through the compressor disk blades and resulting axial loads and increases in air temperature. Analysis of the disk clamps showed safe stress/deflection le..ls at chosen operating speeds.

3.1.2 Optics Adapter

Centered on the test rig top cover is the optics adaptor (Figure 2), providing a 3.81 cm (1.5 inch) diameter hole for mounting the sensor optics tube. The adapter is bolted and spring-dowel pinned to the top cover to provide for accurate replacement when the sensor tube needs to be removed. Set screws are provided to fix the sensor tube position within its mounting hole. The touch probe actuator, provided by NASA, mounts at the center of the adapter and extends down through a hole in the sensor tube. The bottom of the adapter is cut away to allow the compressor blades to pass through the sensor tube axis.

3.1.3 Top Cover Adjustment

The test rig top cover was designed to allow radial adjustment of the sensor optics to simulate changes in rotor/casing clearance. For this, the top cover was designed to hinge at one end and raise/lower at the other end, using adjustment screws (Figure 2). Thus the measureable movement of the end of the top cover is approximately twice the movement at the clearance measurement region, midway between the ends. The error resulting from a true 2 to 1 relationship due to the arc motion is less than 0.15% of expected radial position.
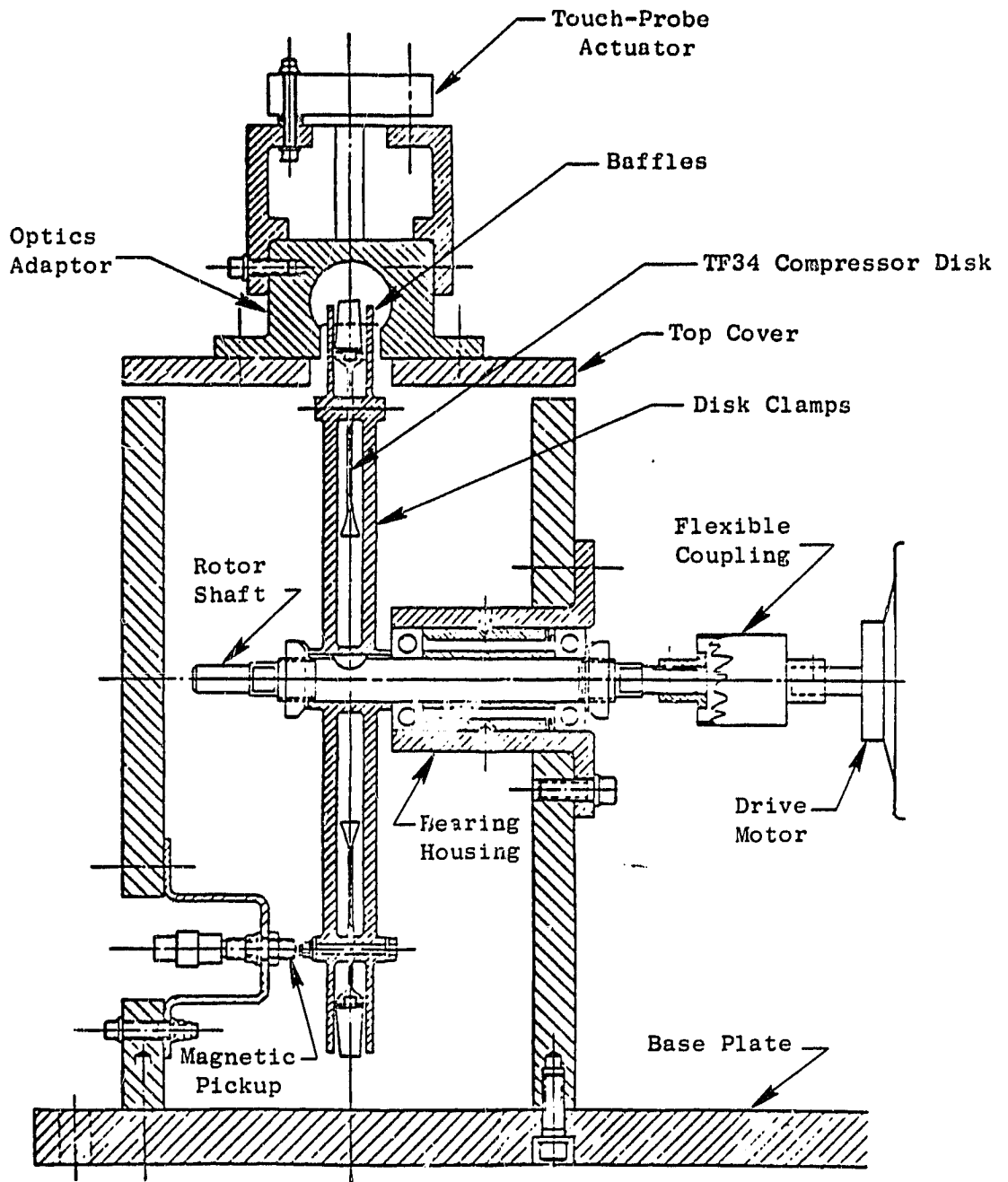
Figure 1. Cross Section of Sensor Test Rig.

4
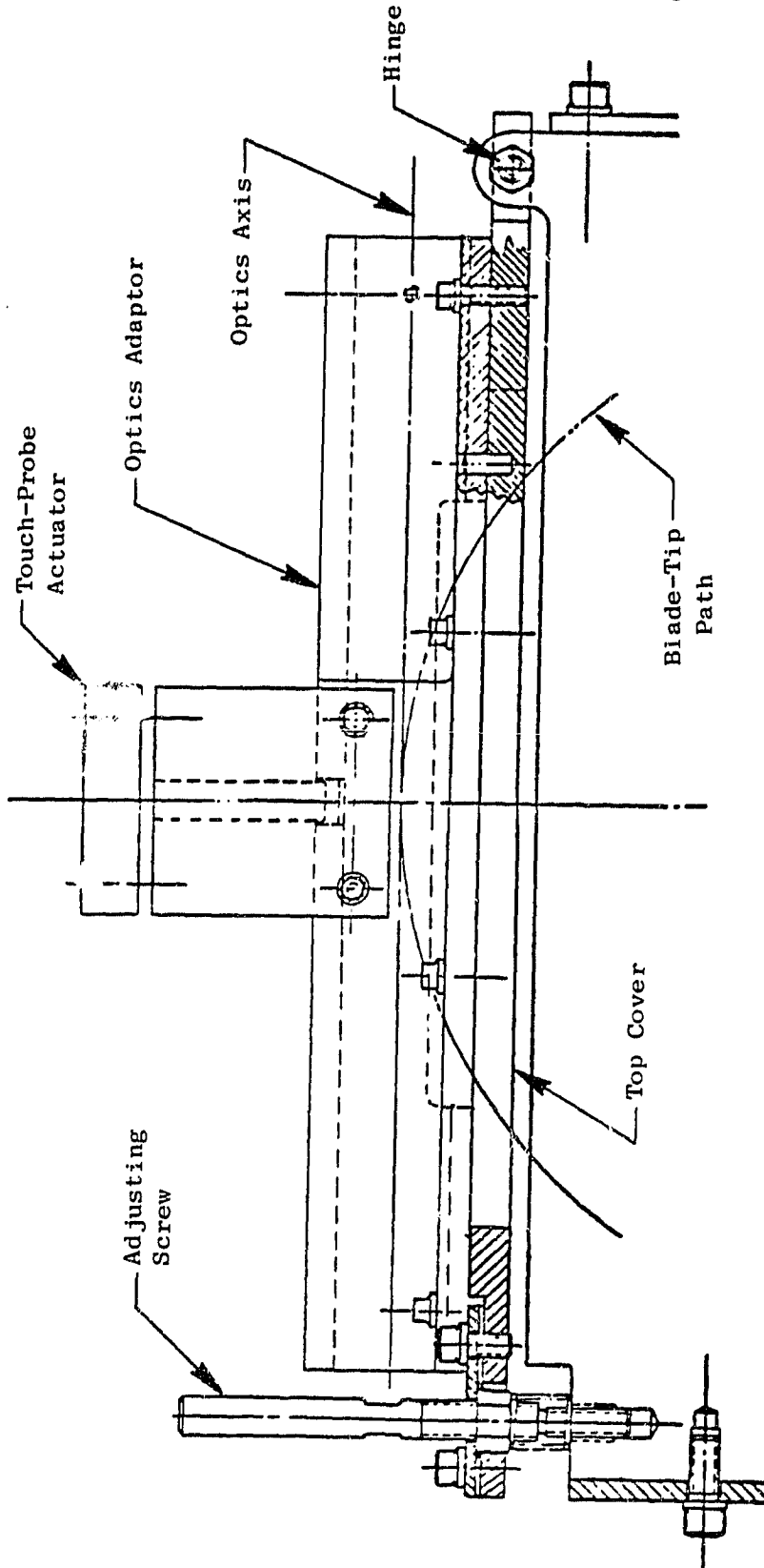
Figure 2. Test Rig Top Cover and Adjustment Mechanism.

The top cover adjusting screws produce micropositioning through the differential thread principle. As the screws are turned into threaded inserts in the test rig end plates, the fixed nut bolted to the top cover travels a slightly larger distance in the opposite direction. The result is a 0.212 mm (0.00833 inches) top cover travel per turn with a $\pm$1.52 mm ($\pm$0.060 inches) total range at the screws, and half these amount at the clearance measurement region. The total travel corresponds to $\pm$7.2 revolutions of the screws. Loading springs are used to help eliminate screw thread hysteresis. Extender bars were added to the adjustment screws to make them easier to turn.

3.1.4 Drive Motor

The maximum speeds obtained by the TF34 engine are in excess of 17,000 rpm. Due to high expected centrifugal stresses and deflections and possibly high windage forces at these speeds, it was decided to design the test rig for a speed of about 10,000 rpm. In addition, this speed appeared attainable with either electric or hydraulic direct drive motors. Measured sensor data could be extrapolated to actual engine speeds. Based on a calculated rotor inertia and a 60 second acceleration time, the acceleration torque required for 10,000 rpm was estimated at 2.16 kilowatts (2.9 hp).

The chosen driver was a universal series electric motor rated at 0.932 kilowatts (1.25 hp) at 7500 rpm with a peak output of about 2.6 kilowatts (3.5 hp). It uses 115 Vac, compatible with speed control using a 15 amp variable transformer. Rotor inertia would greatly reduce any speed variations due to line voltage fluctuations. Upon testing, the motor achieved up to 14,400 rpm unloaded, but only 6000 rpm while turning the test rig rotor with full voltage. This seemed to confirm the concern that windage would have a considerable effect. The major portion of the experiments conducted were run at a motor speed of 1500 rpm, partly because at this low speed the spinning rotor does not make excess noise and partly because effects related to blade and rotor vibration are smaller.

3.1.5 One Per Rev Signal

Due to the principal optical scheme selected for the sensor testing, it was mandatory that the test rig produce a timing pulse once in each revolution of the rotor, in a fixed, known relationship with each rotor blade. This was produced by a magnetic pickup mounted on the inside of a test rig end plate. The pickup position was adjusted so that one bolt in the disk clamp bolt circle, longer than the others, passes within a fraction of a millimeter of the sensor tip. The bolts were chosen to be magnetic for this purpose. A peak-to-peak output of the order of 10 volts (dependent on speed) has been obtained using a gap of about 0.5 mm (20 mils).

6

3.2 TEST RIG SYSTEM

The test rig rotor, including engine compressor disk, disk clamps, shaft, and bearings were assembled and balanced as mounted to the test rig side wall. Figure 3 is a photograph of the assembly. Using a dynamic, two-plane method, the amount of unbalance was reduced to within 2118.4 dyne-cm (0.03 oz.- inches). Contractor drawing number 4013145-902 describes the designed test rig assembly, including a parts list.

A touch probe was received from NASA-Lewis to serve as a reference clearance monitor of the rotor's longest blade. As mounted and operated on the test rig, agreement was obtained between top cover adjustment setting changes, using the adjustment screws, and touch probe reading differences, within about 0.005 mm (0.2 mils), for an 0.107 mm (4.2 mil) change in top cover height (one rotation of adjustment screws).

Figure 4, is a test rig system schematic. Three touch probe extensions run from the actuator to the touch probe control. A 15 amp circuit breaker was added to protect the motor. A piezoelectric accelerometer rated at 44.7 pC/g at 100 Hz and 10g (calibration point) and a charge amplifier were assembled as a safety monitor. Also, safety brackets which shield the rotor/motor coupling interface and overlap the gap under the top cover, were procured and assembled.
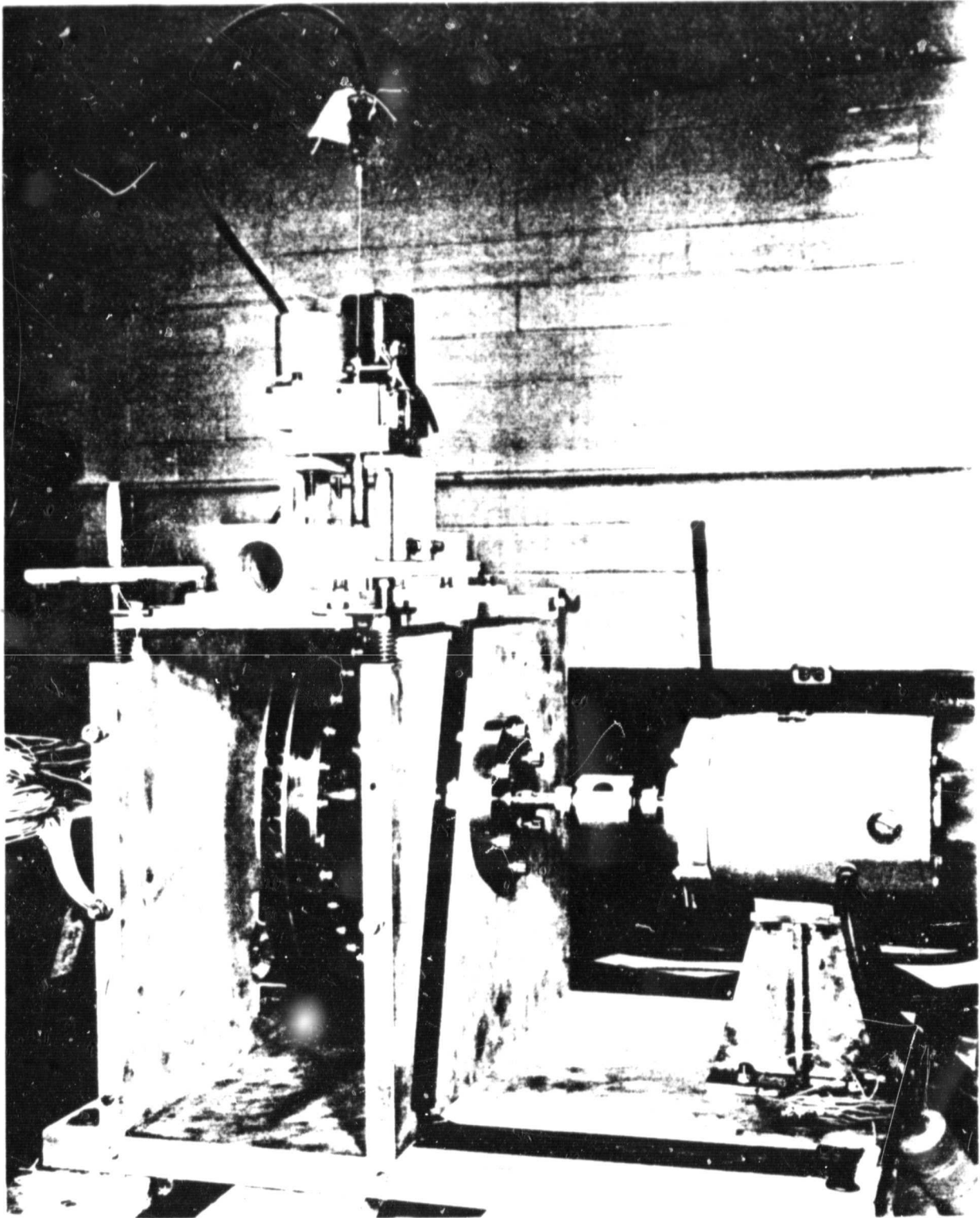
Figure 3. Sensor Test Rig Assembly.

8
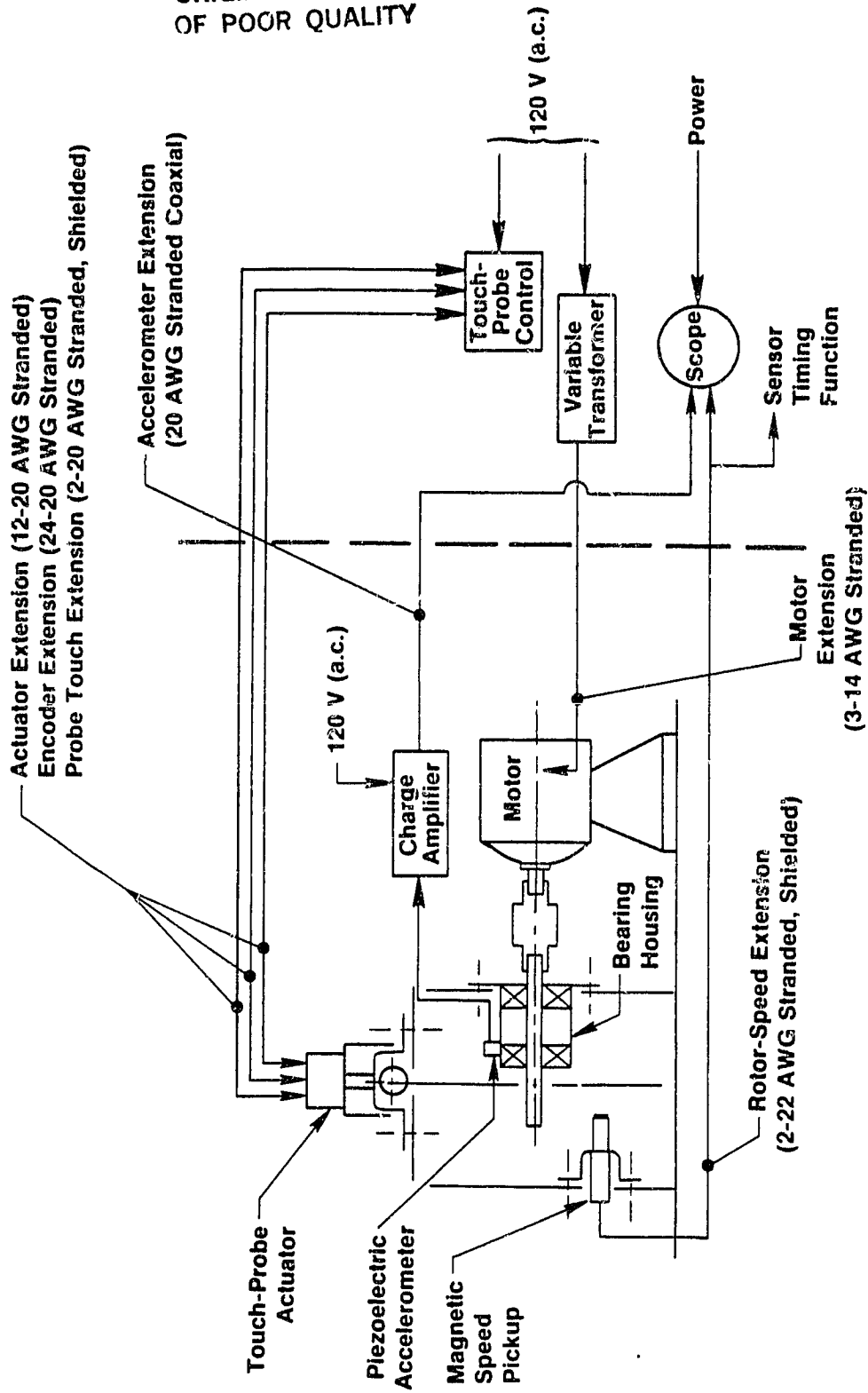
Figure 4. Test Rig System Schematic.

9

4.0 COMPONENT EVALUATION

4.1 INTRODUCTION

Engine environmental temperatures present severe requirements for the sensor components. The contract specified operation at up to 120° C, for the source, detector, and electronic components, 260° C, for optic fiber bundle, and 370° C for lenses or other components exposed to compressor-gas environment. Although the study was intended to determine the feasibility of the sensor and not to test it under on-engine conditions, it was found desirable to identify components which could best meet the on-engine requirements and to test performance, especially at elevated temperature, if essential data were unavailable. Accordingly, elevated-temperature performance tests have been carried out on several components. These include integrity and transmission of an optical fiber bundle tested at 255° C over a period of 3000 hours, decrease in signal from GaAs LED source-Si photodiode combinations on heating from 25° to 125° C, decrease in shunt resistance (and hence noise current increase) in certain Si photodiodes between 25° C and 125° C, and noise-increase and DC output-offset change in a bipolar and in a FET-input operational amplifier. These studies and their conclusions will be presented in detail in the following sections.

4.2 TESTS OF INPUT OPTICAL FIBER BUNDLE

To test the capability of fiber optic bundles at high temperature, a bundle rated for service up to 260° C [1.5875 mm (1/16 in.) bundle diameter, 1.829 m (6 ft) long] was coiled to fit inside a small temperature controlled oven. Radiation from a GaAs LED was focussed into one end of the bundle with a low-power microscope objective while a second objective focussed the emergent radiation onto an phototransistor (used as photodiode). The source, detector, and lenses were kept at room temperature while the bundle was maintained at 255° C. Figure 5 shows the time dependence of the detector output for constant source current. The output decreased to about 83% of the initial value in the first ten hours. Due to the lack of a parallel unheated experiment, it is unsure what part of this decrease can be attributed to settling in of the source or detector. The output decreased very much more slowly for later times so that after 1000 hours it was still 70% of the initial output and 68% at 3000 hours when the experiment was terminated. On removal from the oven the metal sheath of the bundle and the ferrules at the ends were thinly coated with an adherent reddish film, possibly CdO from certain plated screws. However, removal of the film from the bundle tips with dilute HCl did not restore the bundle transmission. The protracted heating caused no obvious mechanical degradation of the bundle.

4.3 LAYERWISE COHERENT FIBER BUNDLES

The basic plan of the sensor required that the output fiber optic bundle consist of several parallel layers of fibers with the fibers in each layer

10
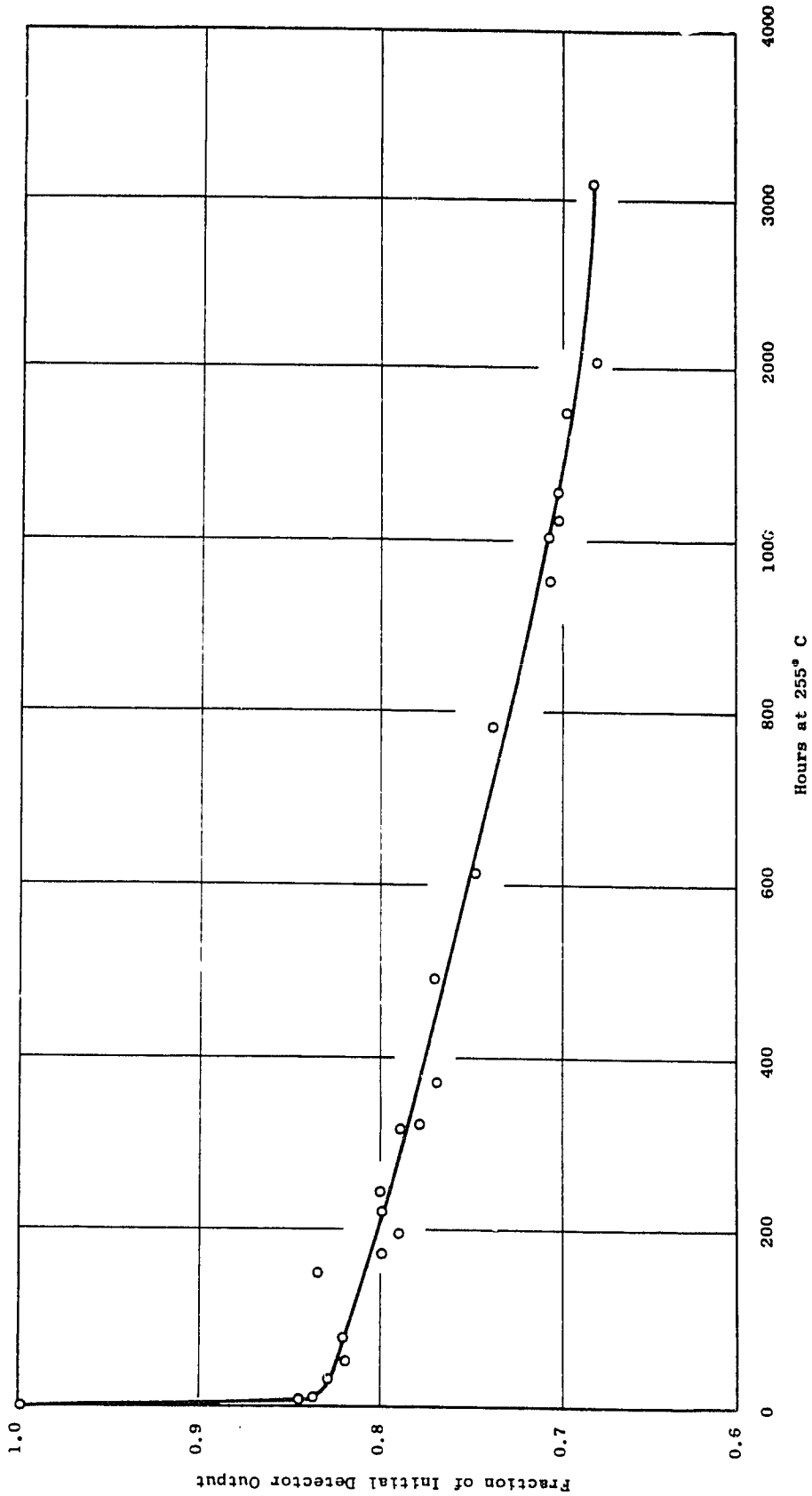
Figure 5.   Transmitted Intensity as a Function of Time for Input Fiber Bundle at 255° C.

11

brought to terminations separated physically by at least a few mm and preferably more. A layerwise coherent bundle design is sketched in Figure 6. The design uses fibers with 38.1 μm (1.5 mil) square cross section. The fibers (and layers) were to be separated by a thin layer of epoxy so that the layer separation would be 38.1 μm (1.5 mils). The fibers for each row would be terminated in a separate 91.44 cm (3 foot) long bundle, the division box being about 3.658 m (12 feet) from the common termination. The epoxies and other materials used have a temperature capability of 218° C (452° F) but the completed bundle has not been tested at elevated temperature.

Figure 7 is a photomicrograph of part of the common end of one bundle. The bright squares are the ends of individual fibers in the four rows receiving visible light at the furcated ends. (The remaining eleven rows can be seen in the photo but are dark because the furcated ends were covered.) The dark squares in lighted rows are individual dead fibers, probably broken. This bundle forms the central element in the feasibility-study sensor.

4.4 TEMPERATURE DEPENDENCE OF SI DETECTOR OUTPUT WITH GaAs SOURCE

The GaAs emitter and Si photodetector were fitted into a small box facing each other, separated by an opal glass diffuser. They were mounted in small teflon sockets so they could be easily changed. This assembly was mounted inside a small temperature-controlled electric oven suitable for operation to 125° C (257° F), with teflon-insulated shielded cables to connect the source and detector to suitable power sources and amplifiers outside the oven. The following units were tested:

1. Spectronix emitter type SE5455-4 with GE Si phototransistor type L14G3 used as a diode in the photovoltaic mode.

2. GE emitter type LED55C with Spectronix photodiode type SC 5425-2 used in the photovoltaic mode.

3. GE emitter type LED55C used with EG+G type PV040 photodiode used in the photovoltaic mode.

Figure 8 summarizes the results. The vertical scale is the (short-circuit) d.c. current produced by the detector with 2 mA source current, and the horizontal scale is component temperature. Although the geometrical arrangement of source and detector was the same for all combinations, the angular distribution of source emission or detector sensitivity was not. Hence no comparison of the absolute results for the different combinations was made. Primarily, these data are presented in one figure for convenience and to emphasize the similarity of the observed temperature dependence. Over the 20 to 125° C range the detector current in all cases decreased by about 1.4% for each degree Centigrade increase in temperature, so that in all cases the current was reduced by about a factor of 3.2 for a temperature increase from 23° to 125° C.

12
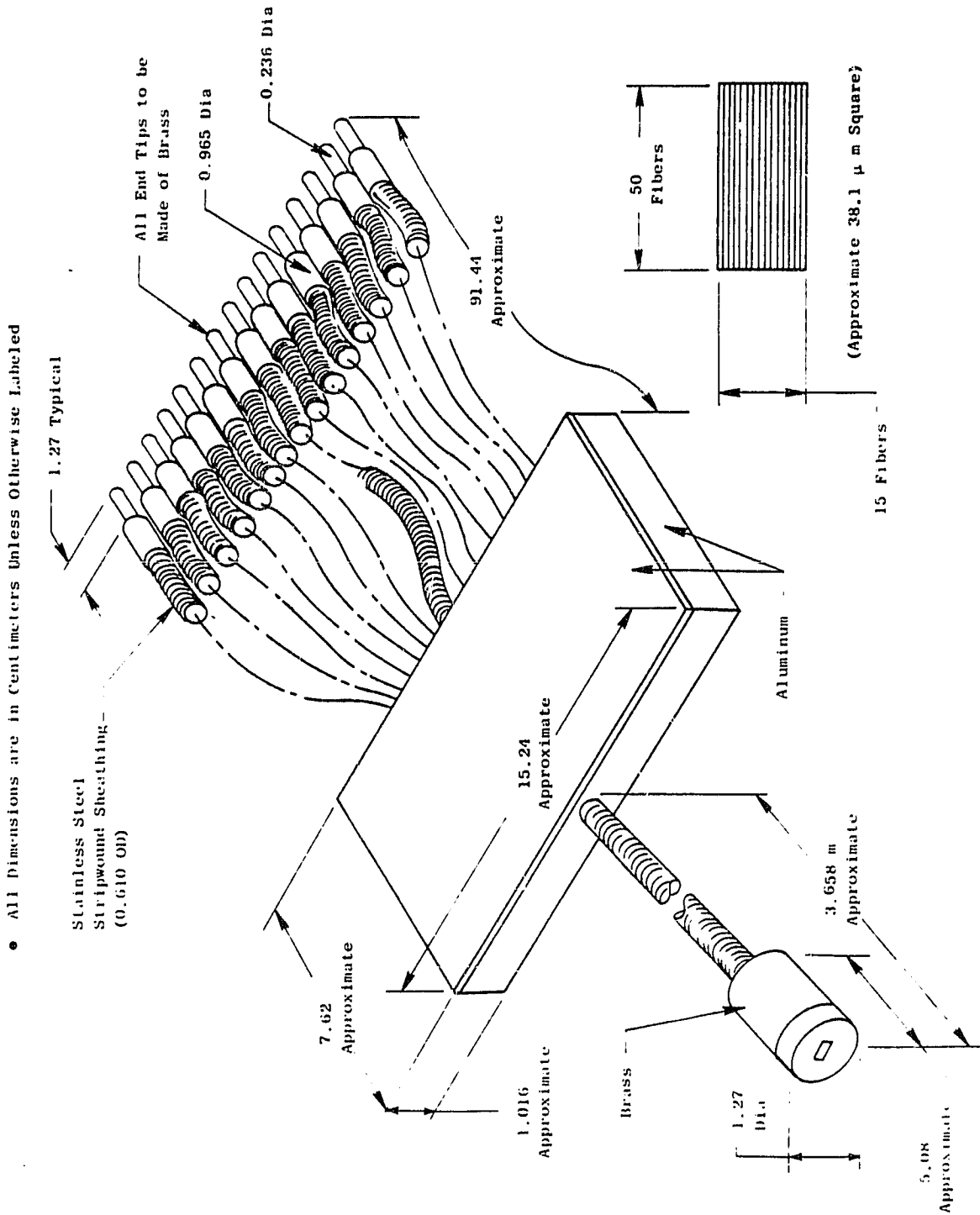
Figure 6. Layerwise-Coherent Optical Fiber Bundle.

13

● Individual Fibers are 38.1 microns (1.5 mils) Square
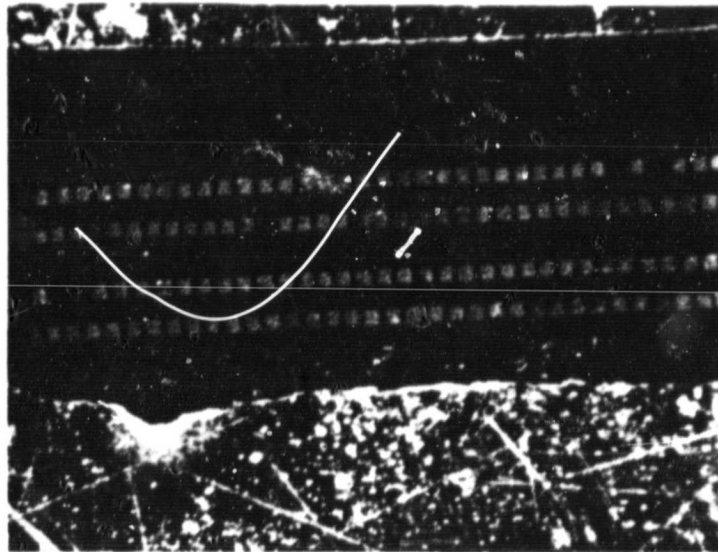
Figure 7. Photomicrograph of Part of the Common End
of the Layerwise-Coherent Bundle.

14
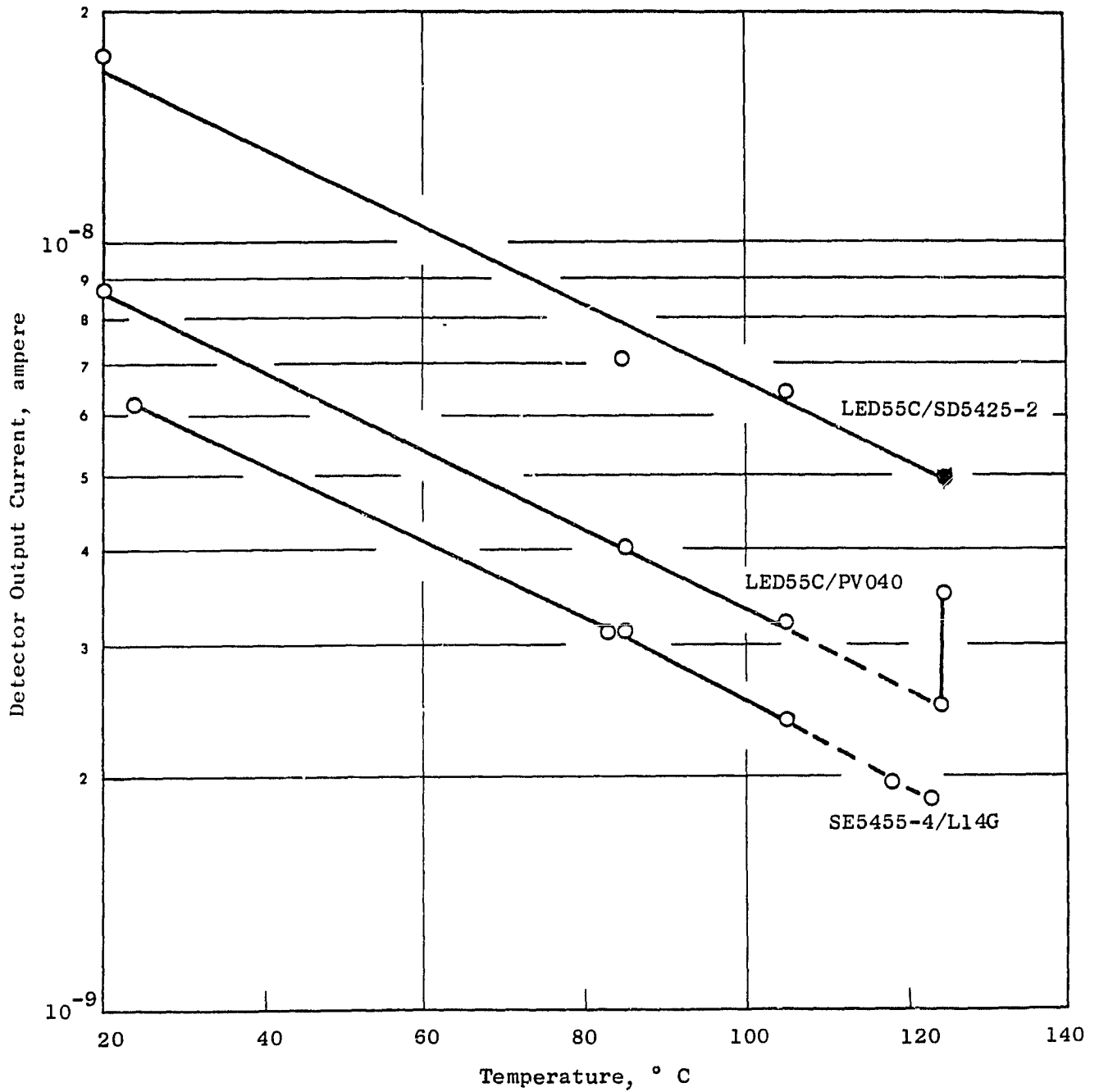
Figure 8. Detector Output as a Function of Temperature for Constant Source Current
for Several Source Detector Combinations.

4.5 TEMPERATURE DEPENDENCE OF THE SHUNT RESISTANCE AND SELF-GENERATED NOISE IN Si PHOTODIODES OPERATED IN THE PHOTOVOLTAIC MODE

The arrangements just described above were also used with the sources turned off (i.e. detectors in the dark) to measure the shunt resistance of the (GE) L14G3, (EG+G) PVO40 and (Spectronix) SD5425-2 detectors at temperatures between 25° and 125° C. A detector may be represented as an infinite-impedance current source in parallel with a shunt resistance, R_s, and shunt capacitance C_s. R_s is related to the density of (extrinsic) recombination centers in the depleted volume of the junction region, while C_s is the junction capacitance across the depleted region, together with lead or other stray capacitance. Thus R_s is high for small detector area (small volume) and low density of extrinsic recombination centers (i.e. high quality material). The thermally-generated mean-square noise voltage generated in R_s is

$$\langle e_n^2 \rangle = 4 \cdot k \cdot T \cdot R_s \cdot (\Delta f)$$

where k is Boltzmann's constant and (Δf) is the bandwidth. The symbol $\langle \rangle$ is used here to denote time average. When e_n is applied across R_s it produces a noise current with mean-square value:

$$\langle i_n^2 \rangle = 4 \cdot k \cdot T \cdot (\Delta f) / R_s$$

so that, obviously, low noise current results when R_s is large. A picoammeter was connected to each detector in turn. This unit is, essentially, an operational amplifier used in the transimpedance mode, and the amplifier input-offset voltage appears at the picoammeter input terminals. This offset voltage (a few millivolts) was measured by the current it produced in a resistance connected to the input. With the offset voltage known, R_s was calculated from the current observed with the photodiode (in the dark) connected to the input. Figure 9 shows R_s as a function of T for the three photodiodes. As expected for thermal generation, R_s is seen to decrease by about a factor of ten for each 25° C increase in temperature.

4.6 TEMPERATURE DEPENDENCE OF OUTPUT NOISE AND OFFSET VOLTAGE IN OPERATIONAL AMPLIFIER USED IN THE TRANSIMPEDANCE MODE WITH Si PHOTOVOLTAIC-MODE PHOTODIODE INPUT

Trials were performed on National Semiconductor Type LM108H (conventional transistor input) and type LF156H (FET input) amplifiers, rated for service at 125° C, for temperature dependence of output noise. Initially, the LM108H was connected as a transimpedance amplifier with a 5.10^7 Ω feedback resistor outside the oven. Figure 10 shows the rms noise from the LM108H as a function of temperature, both with a dummy input and with each of the three detectors
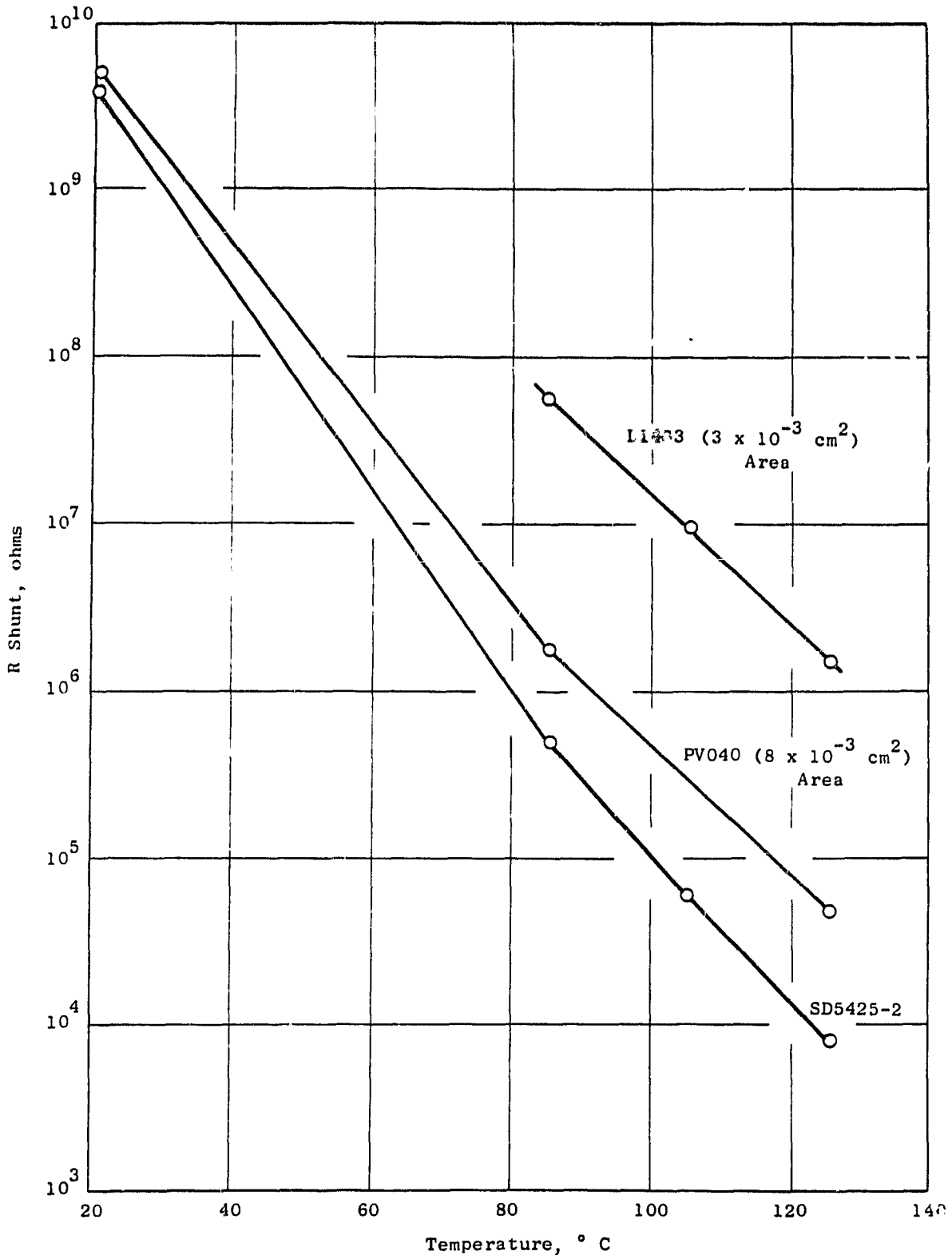
Figure 9. Shunt Resistance as a Function of Temperature for Three
Photodiodes Tested in the Photovoltaic Mode.

17
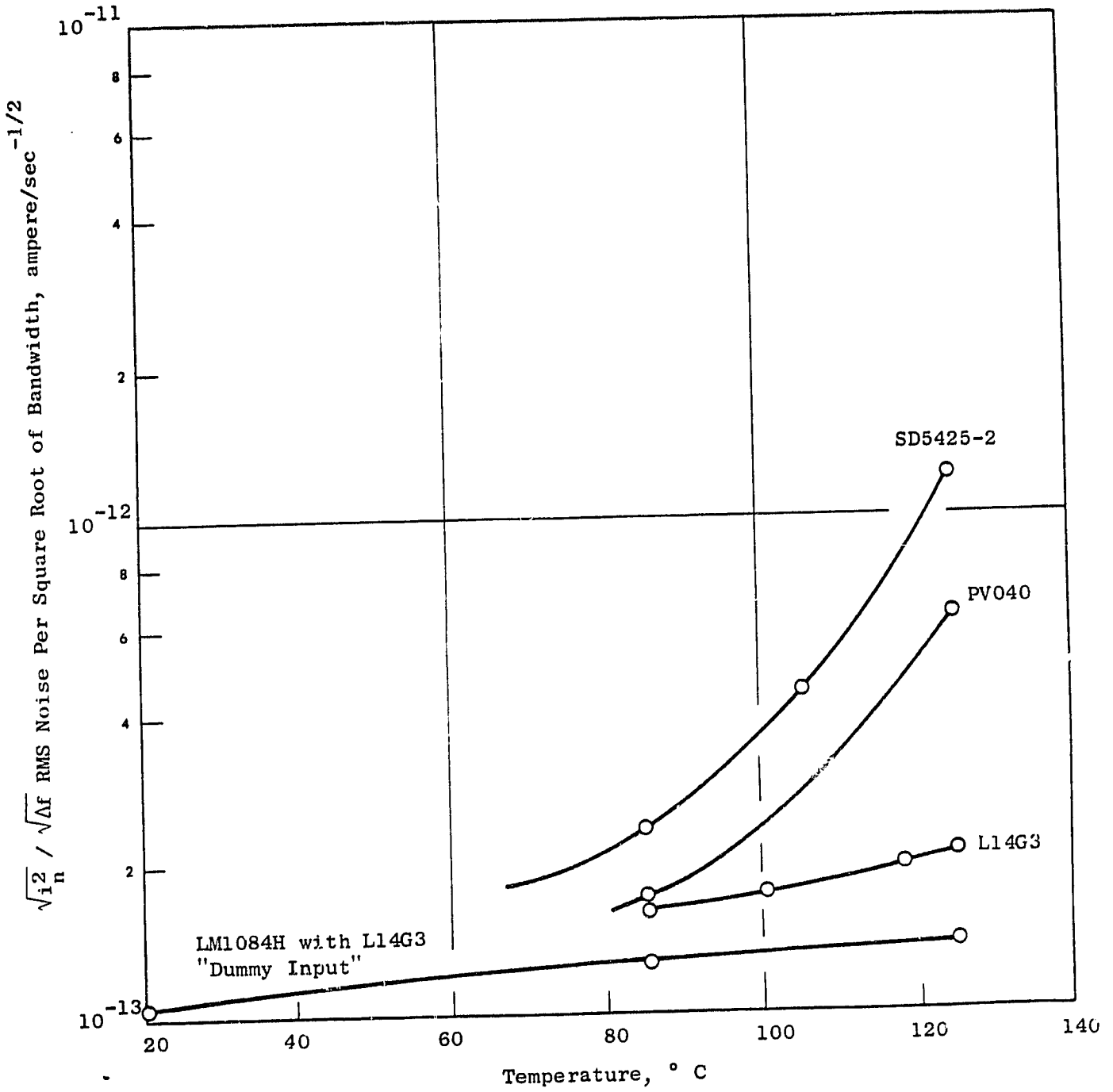
Figure 10.   RMS Noise from the LM108H Amplifier as a Function of Temperature and with Various Detector Inputs.

18

heated along with it. The dummy input was a capacitor selected to give the same noise as the room-temperature detector and amplifier. The noise currents given in Figure 10 were obtained from the observed output noise, divided by the feedback resistance. They show that the LM108H noise increased roughly linearly with temperature and at 125° C was only about 1-1/2 times as great as the room temperature noise. As used with either the SD425-2 or the PV040 detectors, the noise at 125° C greatly exceeds the intrinsic amplifier noise, but with the L14G3, the noise is increased by only a factor of about 1.5 to 1.8 times that at room temperature. Results were about the same for the LF156H amplifier at the 20°, 85°, and 125° C trial temperatures.

Data showed that when heated from 20 to 125° C the output offset voltage of the LM108H with open input changed from 21 to 44 mV, while for the LF156H it changed from near zero (with compensation) to 930 mV. At 125° C, the offset is somewhat different when the L14G3 phototransistor is used (as a photodiode) instead of open input because the input offset voltage flowing through the diode shunt resistance produces a significant input current. Thus with the LM108H, the offset was increased from 44 to 66 mV.

5.0 GENERAL PRINCIPLES IN SENSOR OPTICAL DESIGN

5.1 INTRODUCTION

Figure 11 is a schematic diagram of the sensor showing the fundamental ideas of its operation. Lens L_1 sharply images the input bundle on the blade tip at the instant when it protrudes farthest toward the optic axis, L, (i.e., the axis formed by L_1, L_2 and the bundle centers). Maximum protrusion occurs when the line joining a blade tip and the center of rotor rotation is perpendicular to the optic axis. Similarly, L_2 sharply images the blade tip on the output bundle at the instant of maximum protrusion. The output bundle is specially made with the fibers in distinct layers, the fibers from each layer being brought to a separate detector. At the instant of maximum blade protrusion the number of activated detectors is proportional to the blade clearance. A short blade permits output from more detectors than a long one, and under suitable conditions discussed below the clearance of each blade can be sensed every rotor revolution.

5.2 FUNDAMENTAL GEOMETRICAL CONSIDERATIONS

Figure 12(a) shows the geometry of blade motion in relation to the optic axis. The letter "c" is the center of rotor rotation and "oc" is perpendicular to L. R is the mean radius of the circles that have the largest and the smallest shroud-to-blade clearance; these two limiting radii encompass effects on the clearance caused by blade speed and blade and shroud heating or cooling. Letter "o" is the point of tangency of L with R. The largest and smallest radii differ by 2s. The Greek symbol δ is the (vertical) distance from L to the tip of a blade with radius R, when it is at a (horizontal) distance d from o. Letter "e" is the line between o and this tip. It is seen from the figure that $d/R \approx \tan \theta$ and for small θ, $\delta/d \approx (1/2) \tan \theta$, whence $\delta \approx d^2/2R$.

Consider the case where the source, detector, or both are gated so that signal is produced or sensed only when a blade is at (or very near) o, i.e.. the blade-to-center line is oc. Figure 14(b) shows the configuration at this instant. In addition to the quantities already defined, g is the difference in protrusion between the sensed (vertical) blade and an adjacent blade. The significance of the solid and dashed straight lines in this figure will be explained below.

Figure 13 shows the (approximately parabolic) dependence of δ on d, where for definiteness the blade-tip diameter is taken as 17.78 cm (7 inches) as in the 9th stage compressor of the TF34 engine and in the feasibility-study sensor to be described in the following section. s=0 was assumed for the upper curved line. The lower curved line is the same as the upper except that s=0.5 mm has been assumed. Thus, the circle of radius R + s crosses L at d = 13 mm, when $(\delta - s) = o$. Δ is the downward extent of a lens (assumed to be the aperture stop) which is at a distance D from the maximum-protrusion blade position. From Figure 12(b) it can be seen that $\Delta = D \tan (\theta/2)$. Now

20

Figure 11. Schematic Diagram of Sensor Scheme Explored in this Study.
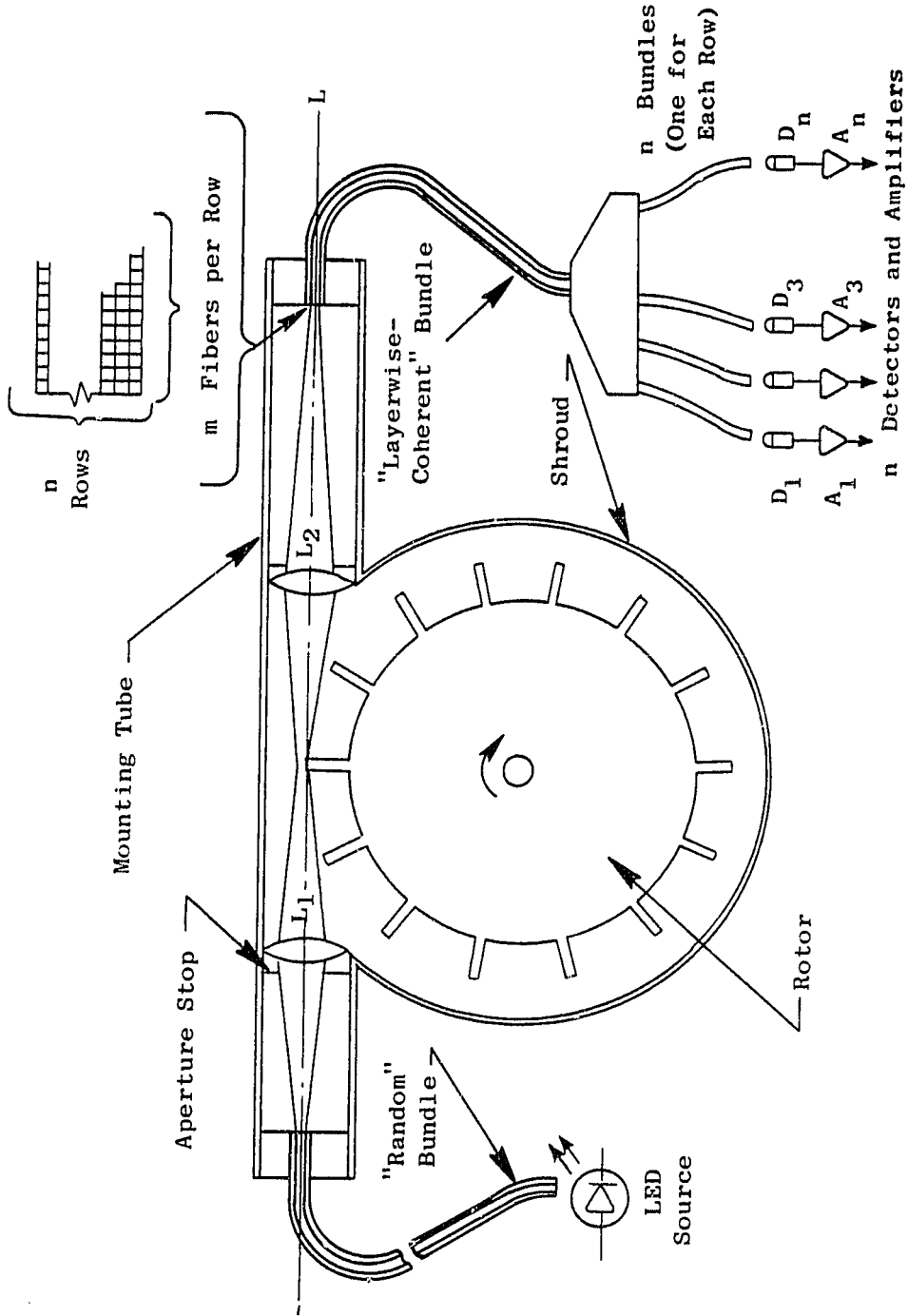
- Lenses and Bundle Ends are Mounted in Shroud.
- Reduction in Clearance Masks LED Emission from More Detectors, When a Blade Tip is Vertical, as Shown.

21

(a) General Blade Position

(b) Blade at Maximum Protrusion and An Adjacent Blade

Figure 12.   Optical and Blade Tip Geometry.
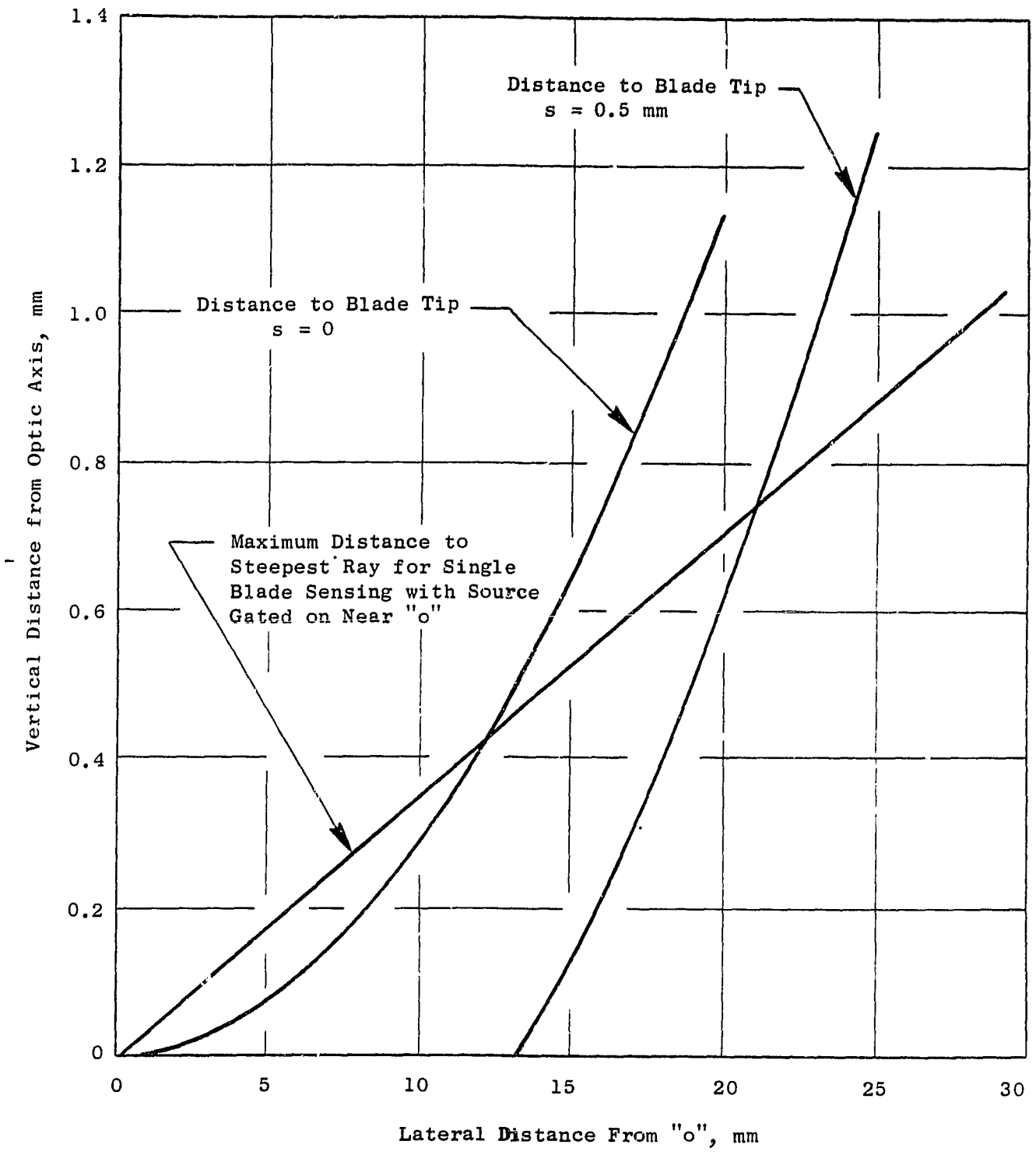
Figure 13. Limits on Vertical Blade to Optic Axis Distance As Related to Blade Clearance and Gating Techniques.

since g is almost parallel to the sensed (central) blade, it is seen from Figure 12(b) that b-g=a, and applying the general result from Figure 12(a), b=A·tan (φ/2) = D · a/A. Here b is the downward distance to an adjacent blade with radius R that is horizontally distant by A.

Two extreme cases can now be distinguished. The first to be considered is g = 0 (all blades of the same height). This case corresponds to the maximum possible angular aperture because the blade tips would cut off from o any radiation at a larger angle. For g = 0, b = a = A·tan (φ/2). The ninth stage compressor already mentioned uses 88 (nearly) equally-spaced blades and the interblade angle is thus φ = 360/88 = 4.091°, and A = 12.7 mm (0.50 inches). The straight line in Figure 13 is drawn with slope tan (φ/2) = 0.03571 corresponding to this steepest ray [and the dashed straight line in Figure 12(b)]. The intersection of this line and the parabola gives the smallest D and Δ for a lens that will not interfere with the blade rotation, assuming s = 0. As discussed below, D and Δ must both be larger if s ≠ 0. (For s = 0.5 mm the non-interference limit is where the straight line crosses the lower curved line.)

For angular apertures less than the maximum just described, the most steeply inclined ray approaches at an angle ψ along the solid line in Figure 12(b). An intermediate case of this type, described in Section 6.0 is where the angular aperture is made exactly half of the maximum. In this case ψ = φ/4 and any value of g that is less than b/2 produces no obstruction of the radiation passing the maximum-protrusion blade tip. Thus it alone influences the intensity. For the ninth-stage compressor just described this corresponds to ψ = 1.046° and the limiting value of g = b/2 is 226 μm (8.9 mils).

In the second extreme case the adjacent blade is assumed to be just enough larger than the sensed blade that it protrudes upwards beyond L far enough to cut off all the radiation from the sensed blade. In this case g = 2A·tan φ/2 and for the 17.78 cm radius, 88-blade case, g = 906.8 μm (35.7 mils). This is the maximum permissible adjacent-blade height for a qualitatively correct indication of the sensed blade, for the maximum angular aperture (g is smaller if the aperture is reduced). The extreme limit for a quantitatively correct indication -- i.e., no adjacent blade interference -- is g = b = 452 μm (17.8 mils), but this corresponds also to zero angular aperture.

5.3   COMPONENT DIMENSIONS FOR FINITE SOURCE AND BUNDLE SIZE; VIGNETTING EFFECTS

Figure 14 shows parameters used in a discussion of lens dimensions in relation to obscuration of source emission in part of the system angular aperture due to the finite lateral size of the source, sensed region, and collector (i.e., vignetting effects). The objective is to calculate the extra size of the optical elements such that the system accommodates the full angular aperture for the marginal rays. In Figure 14, b_1 and b_2 are the diameters of input and output bundles, respectively, p_1, q_1, and d_1 are the object and image distances and diameter of the input lens, and p_2, q_2, and d_2, are the object and image distances and diameter of the output lens. By definition, the lateral

Steepest Ray Through Input Lens
Which Will Clear the Blade and
be Picked Up by Output Lens
for No Vignetting

Input
Lens L1

Output
Lens L2

d_2

Input
Bundle b_1

d_1

θ

θ

s

b_2

Output
Bundle

o

L

p_1

q_1

p_2

q_2

M_1

M_2
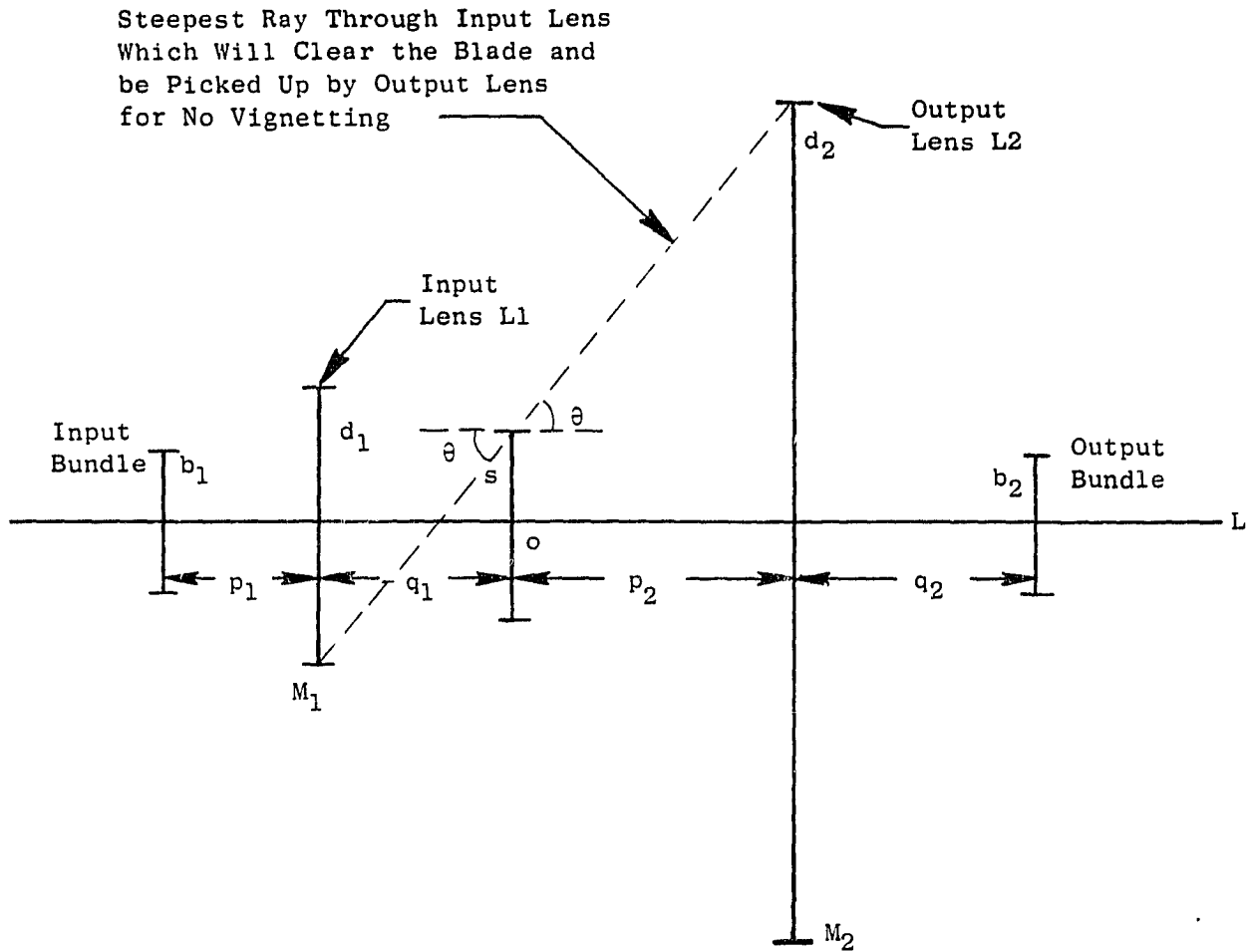
Figure 14.   Schematic Diagram of Lens and Bundle Positions and Sizes
for Discussion of Vignetting Effects.

magnification of the input and output lenses are $M_1 = q_1/P_1$ and $M_2 = q_2/P_2$ respectively. Letter "s" is the total range of variability of the blade-to-shroud distance. In order to fully irradiate this range, $b_1 = s/M_1$ and $b_2 = s/M_2$. Define $k = \tan \phi$ if the system is gated on only near blade vertical. From Figure 14, the minimum value of d_2 for no vignetting is

$$d_2 = p_2 (d_1 + s)/q_1 + s$$

and since

$$d_1 = 2kq_1 \text{ , one obtains}$$

$$d_2 = 2kp_2 + s(1+p_2/q_1)$$

s and k are fixed by the rotor and blade dimensions and operating conditions so that a minimum value of q_1, consistent with maximum permissible aperture, is the value of d from Figure 13 for which the parabola for $(\delta-s)$ intersects the line for single-blade sensing, and obviously this determines a minimum value of d_1. There also is a maximum value of d_2 for blade-clearance. This value is

$$d_2 = (2p_2^2/2R) - s = (p_2^2/R) - s$$

Equating this maximum value to the minimum value above one obtains:

$$p_2^2 = 2R(kp_2 + s) + Rsp_2/q_1$$

If $s = 0$ obviously $p_2 = 2Rk$, but in general the result is more complex. With p_2 determined, the formula for the minimum d_2, above, fixes d_2. M_1 and M_2 are both adjustable in principle, but M_2 is constrained by the blade position digitization increment required, or by bundle dimensions. With M_2 fixed, q_2 is determined. Finally, M_1 is constrained by the angular range of the bundle and source and also by the source size and uniformity of its emission.

5.4 DIFFRACTION LIMITATIONS

As in any (imaging) optical system, the sharpness of the blade-tip image formed by L_2 on the layerwise-coherent output bundle is limited by diffraction effects and lens abberations. In the present case the source is almost monochromatic and the angular aperture is small so that diffraction effects should be far more important than abberations. Diffraction effects are an essential manifestation of the wave nature of light and are controlled by the form and dimensions of the optical system, especially its angular aperture. An exact calculation of the diffraction-induced smearing of the blade-tip image is possible but the geometry does not exactly correspond to any of the

26

testbook cases and as shown in Figure 15, the following simplifications are
made:

1.   The blade tip is considered to be a line source at S

2.   w is the width of the aperture stop. This is the width of the lens
      if it forms the aperture stop in the actual sensor, or it is the
      narrower of the two dimensions of the rectangular aperture if a
      separate stop is used as in the feasibility study sensor. Diffrac-
      tion effects are also produced by the longer-dimensions of the lens
      or separate stop, but these are smaller and neglected here.

With these simplifications the standard results for Fraunhofer diffraction
by a slit apply exactly (Reference 1 or 2). Qualitatively, the image of the
line source (blade tip) is expected to be broadened symmetrically on either
side of L and weak secondary intensity maxima are produced. With slight re-
arrangement the results in the two references above give:

$$y = k \ p_2 \ \lambda/w$$

k = 1.00 gives y at the first minimum while k = 1.43 gives y at the first secon-
dary maximum. k ≈ 0.42 gives y for a 50% decrease from the central maximum in-
tensity, while k ≈ 0.54 corresponds to a decrease from about 90% to about 10% of
the central intensity. Obviously also y is inversely proportional to the angu-
lar aperture ($\approx w/p_2$).

Figure 16 is a diagram of the apparatus used to investigate the sharpness
of the image of a razor blade produced with the optical components used in the
feasibility study sensor described in the next section. The first pair of
microscope objectives formed an image of the lamp on the razor blade that simu-
lates the blade tip. Then the second pair formed an image of the blade which
was relayed to the camera film by a 450X microscope, where a greatly magnified
image of the blade edge was formed. The angular aperture was a 2.6 mm width
slit with the width dimension perpendicular to the blade edge. (All these
dimensions were the same as in the feasibility study sensor). Careful align-
ment and focus adjustments were essential.

Two exposures were made on each negative with the blade edge moved 101.6μm
(4 mils) between exposures. The separation of the two images on the film con-
veniently calibrated the magnification. The photographs were not measured with
a photometer, but visual examination indicated the intensity decreased from
nearly 100% to about 50% in a distance corresponding to about 7.62 to 11.43 μm,
for 535 nm radiation. The corresponding broadenings at 900 nm should be 12.7
to 19.3 μm. Similarly, at 535 nm, the intensity decreased from about 90% to
about 10% of the no edge value in 6.86 to 9.14 μm, corresponding to 11.68 to
15.49 μm at 900 nm. These measured broadenings exceed the results of the
simple Fraunhofer-diffraction theory by a factor of 1-1/4 to 1-3/4, which is
thought to be very satisfactory agreement considering the limitations of the
theory and nature of the experiments.
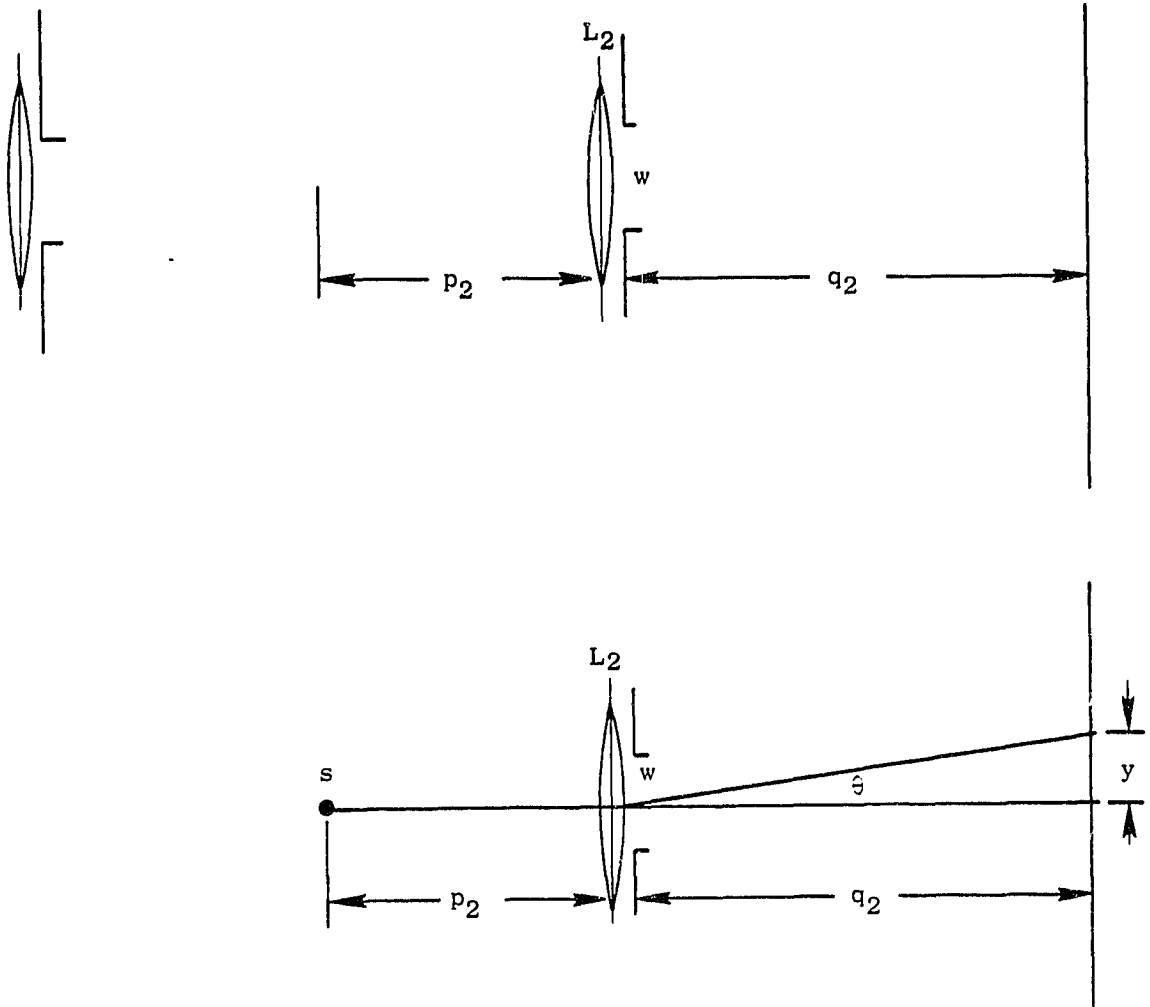
Figure 15. Diagram of Actual Optical System (Upper) and Simplified
Optical System (Lower) for Discussion of Diffraction
Theory.

Figure 16. Experimental Arrangements Used for the Study of
Diffraction Effects.
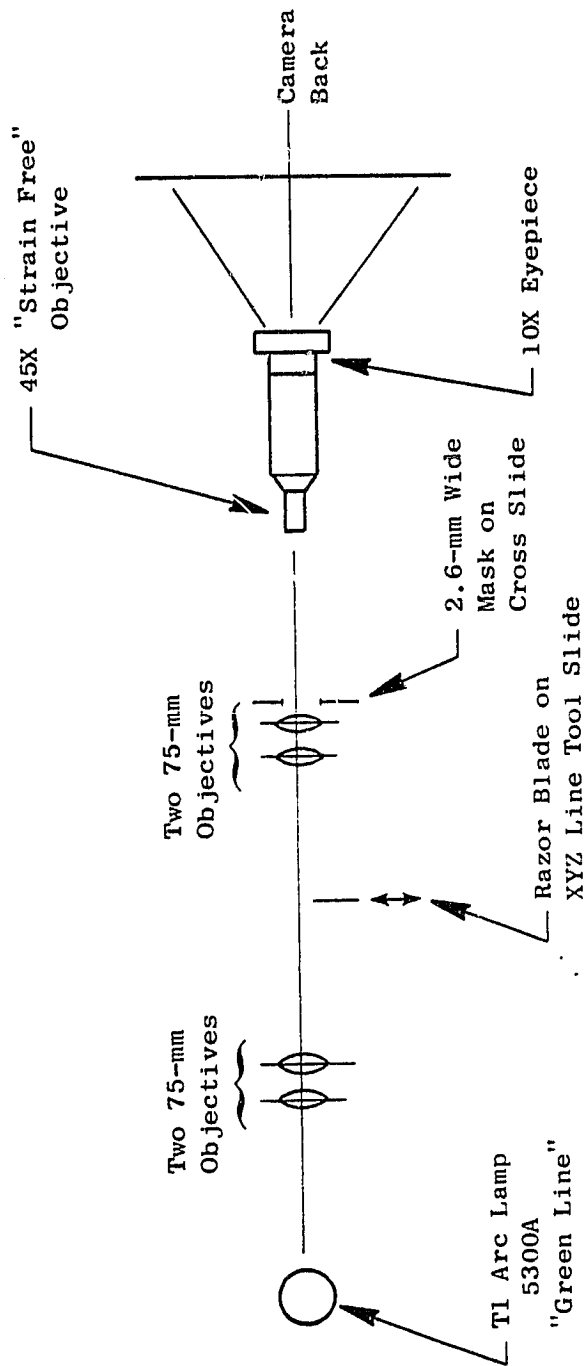
Note: Lamp positioned to be focussed on razor blade. Razor blade
(and microscope) positioned to get "best" image in microscope
with approximately equal image and object distance.

6.0 DESIGN OF THE FEASIBILITY STUDY SENSOR

6.1 OPTICAL COMPONENTS AND MOUNTING TUBE

The general principles developed in Section 5.0 were applied to the design of a sensor to study the feasibility of this approach for measuring blade tip clearance of the spin rig rotor described in Section 3.0. In this feasibility study sensor design, no attempt was made to keep D_1 or D_2 small. L_1 and L_2 are flat-mounted microscope objective lenses selected for their optical suitability, availability, and relatively low cost, rather than their suitability for a highly compact design. The essential parts of two sensor designs intended to have much smaller, (near-minimum) size are given in Section 9.0.

For simplicity and rigidity all the optical elements of the sensor are mounted coaxially in a thick-walled tube in such a way that essential adjustments can be made first with the tube out of the spin rig and reproduced after installation. At the outset it was decided to design the sensor so as to easily obtain unity, two-fold, or three-fold magification of a maximum-protrusion blade on the layerwise coherent output bundle. Since the bundle layer separation is 38.1 µm (1.5 mils), blade tip clearance digitization intervals of 38.1 µm (1.5 mils), 19.1 µm (0.75 mil), or 12.7 µm (0.5 mil) are thus easily obtained. For unity magnification L_2 uses two 75 mm f.l. flat-mounted microscope objective lenses mounted closely spaced with the pair about 75 mm distant from the blade-tip or bundle. These lenses are designed to work with the image distance q = 160 mm rather than ∞, but the aberration increase, though detectable, is not important with the angular aperture reduced as discussed below. Two-fold magnification is obtained with a 50 mm f.l. objective used with p_2 = 75 mm and q_2 = 150 mm, so that little abberration increase is produced. Three-fold magnification is also obtained with the 50 mm f.l. lens but with p_2 = 66.6 mm and q_2 = 200 mm. All of these lenses are mounted in 2.54 cm (1 inch) OD holders with insides threaded to accept standard microscope objective threads. For the 88-blade 17.78 cm (7 inch) diameter spin rig rotor, ϕ = 4.091 and the results in Section 5.0 give Δ = 12.6 mm for D = 67 mm, and 15.8 mm for D = 75 mm. Thus with the mounting tube inside radius of 1.27 mm there is ample clearance for the lenses and mounts with unity and two-fold magnification and minor machining of one of the lens mounts gives adequate clearance for the lens position for three-fold magnification.

Figure 17 is a drawing of the 6061 aluminum alloy tube used to mount the optical components. The tube was heat-treated before machining to stabilize its dimensions. The cut-out section best seen in the side view provides clearance for the blades in the rotor. The recessed holes and slots seen in the top view are used to hold the mounted optical components. Screws through the holes "A" hold the lens mounts while the slots "B" are used with the input and output bundle mounts and provide focus adjustment. All components are mounted with their centers coincident with the tube axis.

Figure 17. Tube Used for Mounting Optical Components in Feasibility Study Sensor.

31

As noted in Section 5.0, the angular aperture of the optical system has an important relation to its performance. In the study setup the aperture is controlled by a plate with an essentially rectangular hole and is mounted between the lenses in either lens holder (or in both holders). Selection of this aperture is a compromise: increased signal (and hence better signal-to-noise ratio) and smaller diffraction smearing of the blade-tip image result with larger aperture, while reduced sensitivity to adjacent-to-sensed-blade protrusion difference results with smaller aperture. When used with $p_1 = q_1 = 75$ mm, this aperture, 2.6 mm, is (almost) exactly half the maximum permitted for pulsed source operation as discussed above. Thus, as already noted, if the fiber-layer thickness is ignored, an adjacent blade can be as much as 226 μm (8.9 mils) higher than the sensed blade without reducing the beam at the sensed blade, or looked at in another way, the sensed blade can be 226 μm (8.9 mils) shorter than an adjacent blade without affecting the signal produced when the shorter blade is at maximum protrusion. Obviously, choice of this aperture is, within limits, an arbitrary compromise between independence of sensing and detector response.

The special layerwise coherent fiber bundle is used as the output bundle. A 1.829 m (6 foot) long cable is used as the input bundle for the GE LED55C GaAs LED source. Fifteen L14G3 phototransistors, used as photodiodes, serve as detectors. Each detector is mounted in a bundle-to-detector coupling module shown in Figure 18. These modules have the advantage of simplicity and low cost, but provide no lateral bundle-to-detector position adjustment.

6.2 TESTS OF THE OPTICAL DESIGN WITH A TIP SIMULATOR

A preliminary evaluation of the performance f the feasibility study sensor was obtained by setting up the optical system together with a tip simulator that could reproduce the motion of five adjacent blades in the actual rotor. Figure 19 is a photograph of the entire arrangement showing the source, input bundle and optics, tip simulator, and an output bundle coupled to a detector, while Figure 20 shows the tip simulator, lenses, and an aperture stop more clearly. At the time this study was undertaken, the layerwise coherent output bundle had not yet been received and so it was simulated by a spectrometer slit adjusted to 38.1 μm (1.5 mils) width and 1.905 mm (75 mils) length as in the actual bundle. This slit can be seen in Figure 19 as can a second bundle placed behind the slit to carry the emergent radiation to an L14G3 phototransistor, used as a photodiode in the photovoltaic mode, as in the feasibility study sensor. The diagonal bars were adjusted to be equidistant from the common center of rotation on the rotation-translation stage within ±5.08 μm (0.2 mils). A micrometer screw allowed translation of the whole simulator bar assembly in a direction perpendicular to the optic axis, while a motor driven screw allowed the tips to be rotated in slow simulation of the motion of compressor blade tips.

Ferrule to Hold
Connector

Brass Tube

Phototransistor
Socket

Ferrule to Hold
Bundle Tip

Miniature
rf Connector

L14G3 Phototransistor
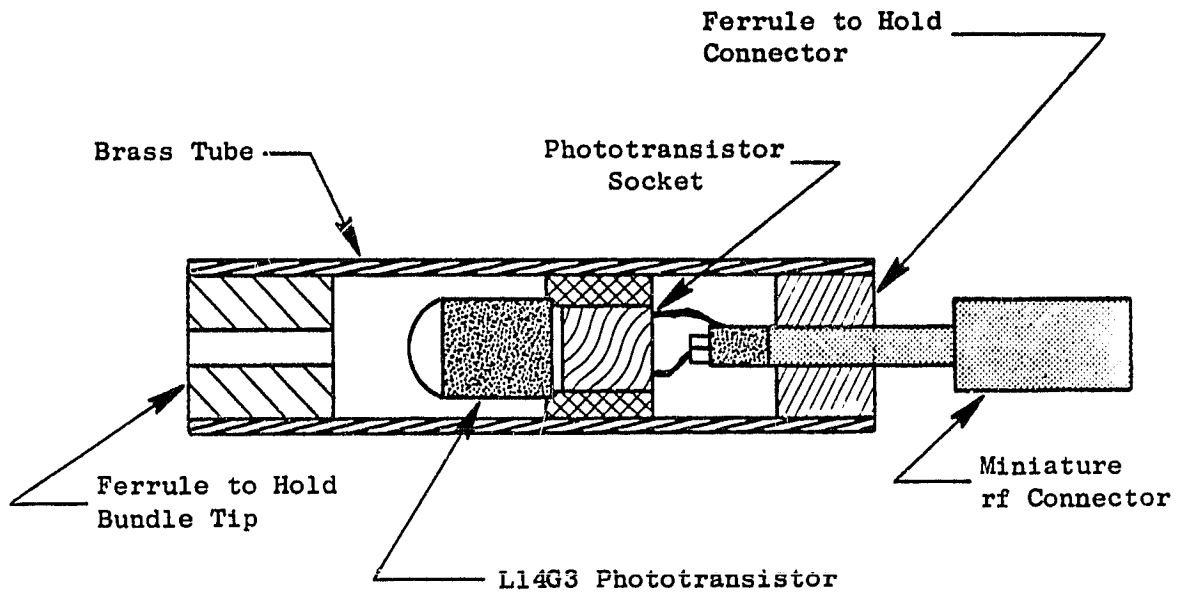
Note: Approximate Scale 2/1.

Figure 18.   Cross Sectional View of Bundle-to-Phototransistor Coupler.
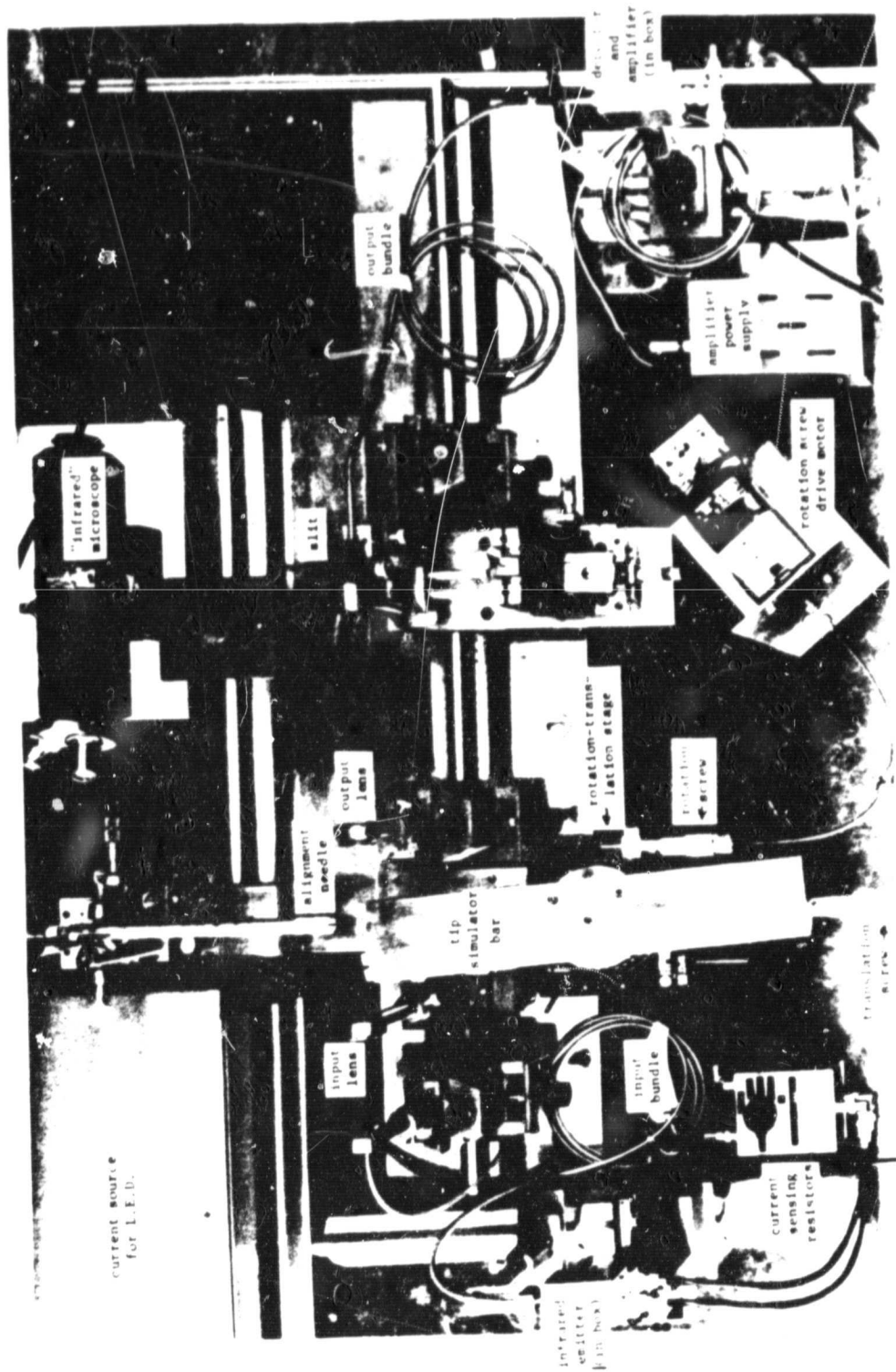
Figure 19. Optical Sensor System Simulation Assembly.
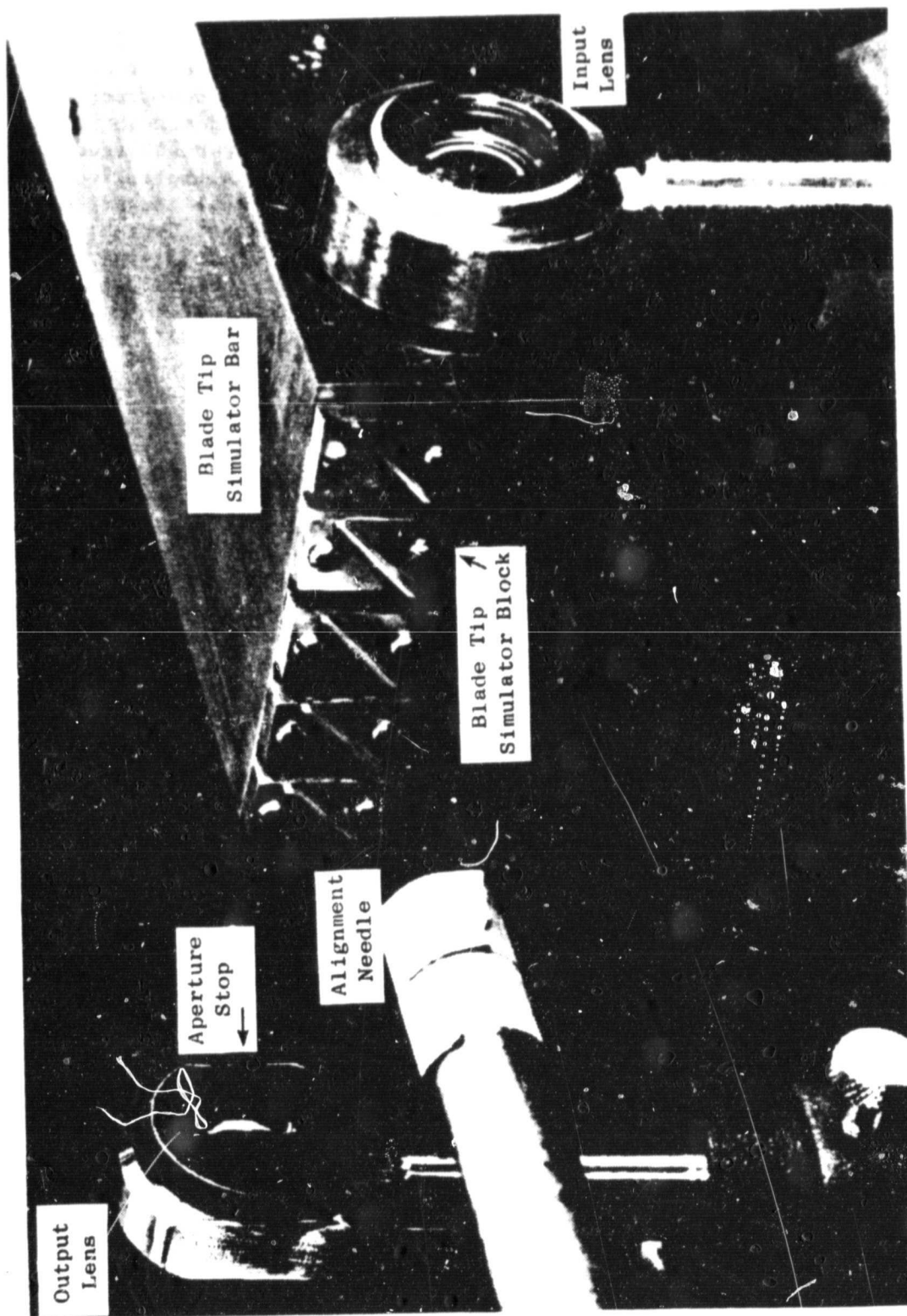
Figure 20. Tip Simulator, Lenses, and Aperture Stop of Optical Sensor System Simulation.

Input Lens

Blade Tip Simulator Bar

Blade Tip Simulator Block

Aperture Stop

Alignment Needle

Output Lens

35

Figure 21 shows records of the intensity as a function of simulator-tip angle for four different insertions into the beam. Comparing 21(a) and 21(d) one sees that 0.06 mm (2.4 mils) increase in insertion reduces the detector response at maximum blade protrusion from about 90% of the unobstructed value to less than 1%. For convenience, these data were obtained with a pulsed-source mode of operation but are essentially equivalent to DC source results. Comparing Figure 21(a) and (c) one notes that secondary maxima in Figure 21(a) coincide with the minima in 21(c). This shows that for small insertion, the attenuation at maximum protrusion is (slightly) less than with the blade at a small angle, as expected in this case from geometrical optics alone. Records similar to those in Figure 21 were seen with the actual rotor as will be discussed below. Results obtained with the simulator were helpful in planning the operation of the feasibility study sensor long before it was completed.

6.3 ADJUSTMENT OF THE FEASIBILITY STUDY SENSOR OPTICS

Adjustment of the components for unity magnification will be described but adjustment for twofold or threefold magnification follows the same general procedure. As the first step, the optics tube was mounted horizontally on an optical bench with the input pair of 75 mm f.l. lenses and the aperture plate in their normal positions. A simple micromanipulator was used to move a needle into the correct position for the center of a maximum-protrusion blade, namely, laterally centered in the tube and, longitudinally, with the needle tip in the middle of the touch-probe slot. The needle was irradiated with an incandescent lamp filtered so that only wavelengths longer than about 750 nm were included. Then an infrared microscope operated at 20x and mounted with its axis horizontal was adjusted so that the needle tip appeared in sharp focus. As the image-to-lens distance of the microscope had been previously measured, this located the correct position for the end of the input bundle. Without disturbing the microscope, the two 75 mm f.l. output lenses and the output bundle were installed (the needle irradiating lamp having been removed). Radiation from the filtered lamp (or from a LED55C emitter operated with 100 mA DC) was now introduced through one of the fifteen output bundles so that a line of fibers emitted infrared. The longitudinal position of the bundle was now adjusted so that this line appeared in sharp focus, with the image of the output-bundle-tip exactly vertical, i.e. perpendicular to the axis of the touch probe slot as adjusted by rotation of the bundle in its mounting cylinder. This correct position of the output bundle mounting cylinder screw was then marked on the optics tube. (Because of the narrow angular aperture such marks made possible reinstallation of either bundle with adequate accuracy). The output bundle in its mounting cylinder was now removed from the optics tube. The tube was then positioned in the adapter plate so that the touch probe slot was longitudinally centered on the round touch probe hole in the adapter plate with the axis of the optics-cylinder mounting screws inclined about 2.5° to the vertical so that the output bundle fiber rows were parallel to the blade tips. The optics tube was finally clamped into the adapter plate with the two set screws and the fiber bundles (in their cylinders) were installed.
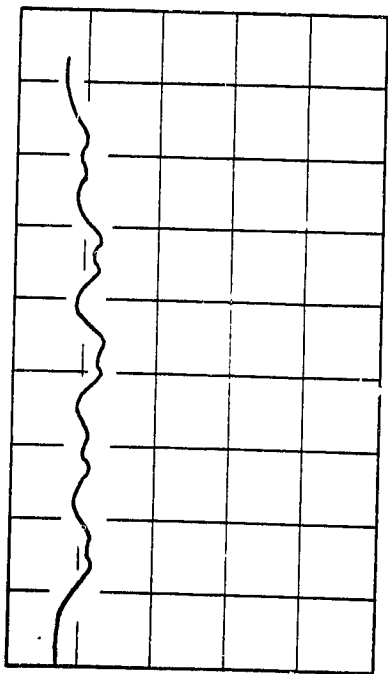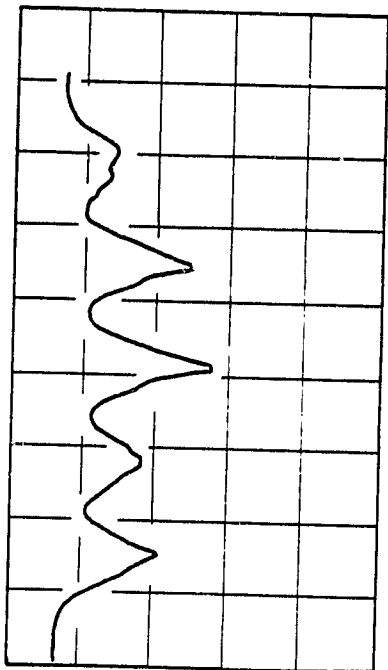
(a) "Insertion" = 0.29 mm

(b) "Insertion" = 0.275 mm
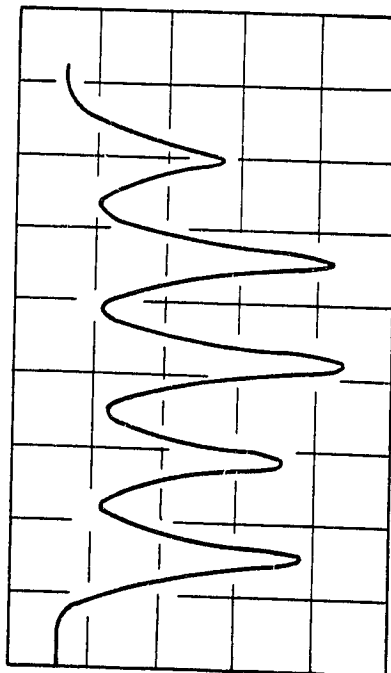
(c) "Insertion" = 0.26 mm
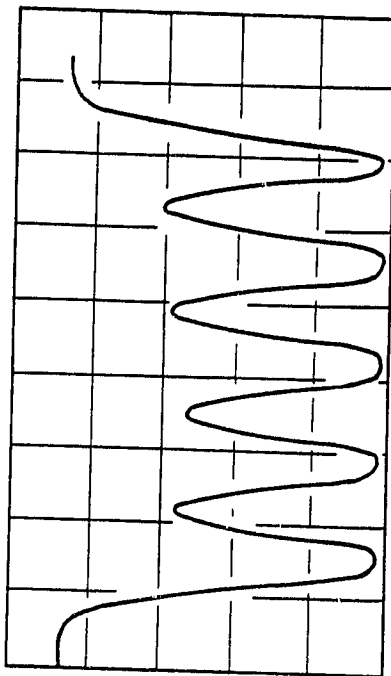
(d) "Insertion" = 0.23 mm

All Runs: Input and Output Aperture Stops 2.6 mm Wide, Approximately 12 mm Long
Input Lens—Two 75 mm f.l. Close Spaced
Output Lens—One 50 mm f.l. Operated with 2x Magnification
Exit Slit—38.1 μm (1.5 mils) Wide, 1.905 mm (75 mils) Long
Source—LED 55CF 400mA 10 μsec Pulses, 1msec Rep. Time
Signal from Detector with Unobstructed Beam = 1.8 x 10⁻⁸ A

Figure 21. Detector Response as a Function of Blade Tip Angular Position as
Observed with Simulator.

7.0 OPERATION OF THE FEASIBILITY STUDY
SENSOR WITH THE SPIN RIG

7.1 DIRECT CURRENT SOURCE OPERATION

7.1.1 Trigger-Pulse Generator for a Selected Blade

Our initial experiments were measurements of the detector response (radiant intensity) for each layer of fibers, (hereafter called a channel), as a function of time, for direct current, (DC) operation of the LED55C source (at 50 ma), 1500 rpm rotor speed, and with L_2 adjusted to give twofold magnification of the blade tips at the output bundle. These experiments were greatly facilitated by development of a special trigger-pulse generator by Dr. H.H. Woodbury (General Electric, R&D Center).

As noted in Section 3.0 the magnetic pickup produces one pulse every rotor revolution with the pulse occurring as the blade loading slot passes under the touch-probe hole. These rotation-sensor pulses control the generation of BLADE-SYNC pulses that have variable phase-decay so that a trigger pulse can be made synchronous with the sensing of any selected blade, almost independent of rotor rotation rate. The circuit diagram of this variable-period divider is explained in Appendix A, Figure 33.

In the DC-source experiments, oscilloscope triggering by the BLADE-SYNC pulse in the single mode allowed the start of the oscilloscope display to coincide with any desired blade, while the sweep speed of the scope could be adjusted so that a full screen sweep corresponded to any desired number of blades. It should be mentioned that all blade numbers in this report are given according to the convention that when the rotor is viewed from the motor side and the loading slot is at the top, the blade just to the right of the slot is number one with the numbers increasing clockwise around the rotor so that 88 is also adjacent to the slot but at its left. The spacing of the blades is · nearly, but not quite, uniform as will be discussed below. The gap between blade 1 and No. 88, common in compressor rotors, is about 1-1/2 times as large as between any other pair of blades.

7.1.2 Rotor Blade Height Characteristics Observed

In the spin-rig rotor, not typical of an engine quality assembly, there is an average eccentricity in the protrusion of the blade tips as measured from the center of rotation. Blades in the No. 20 to No. 30 range protrude roughly 203 µm (8 mils) farther, on the average, than those in the No. 60 to No. 70 range. In addition to the average eccentricity, there are substantial adjacent-blade protrusion differences. These differences are evident in the results shown in Figures 22 and 23. These are also photographs of the oscilloscope screen, but the phase delay of the BLADE SYNC pulse was adjusted so that the sweep starts just as blade No. 8 is coming to maximum protrusion, with the sweep speed increased so that the time for one blade (about 455 µsec at 1500 rpm) corresponds to one square. Comparison of the modulation produced by

38

Blade No. 8 9 10 11 12 13 14 15 16 17
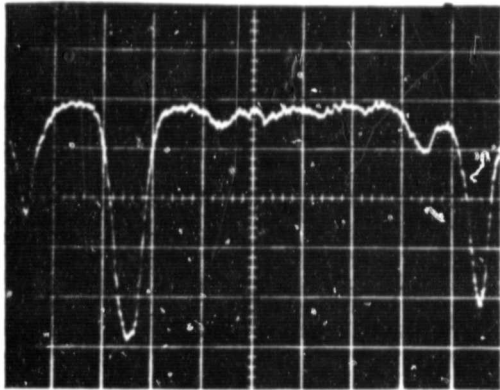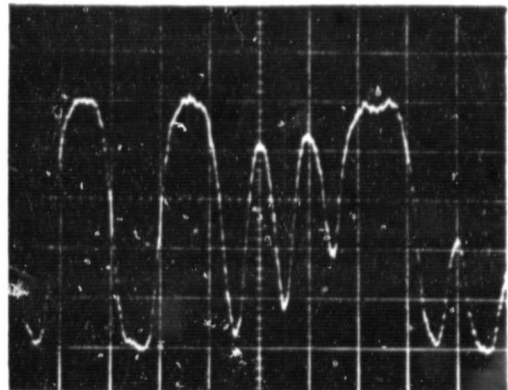
528   Ch #2

528   Ch #5
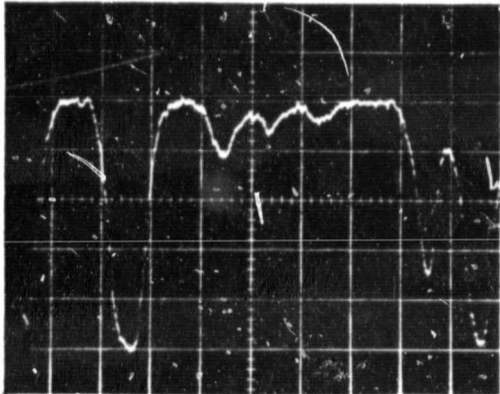
528   Ch #3
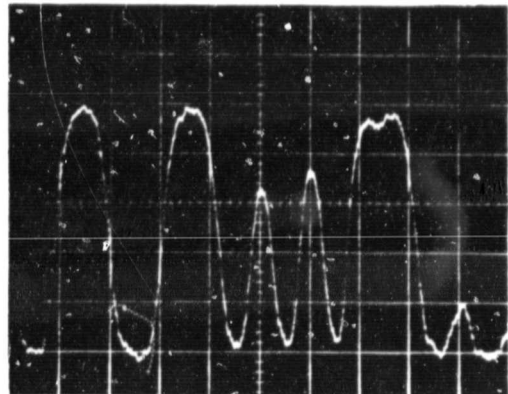
528   Ch #6
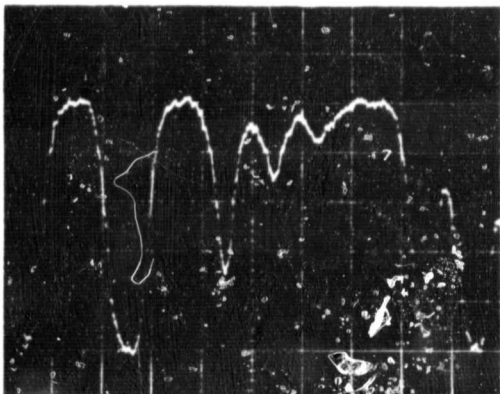
528   Ch #4
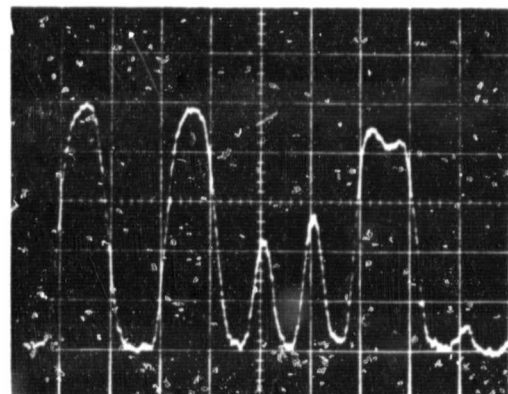
528   Ch #7

Figure 22.   Detector Output for a Nine Blade Spread - Channels 2 Through 7.

Blade No. 8 9 10   11 12 13 14 15 16 17
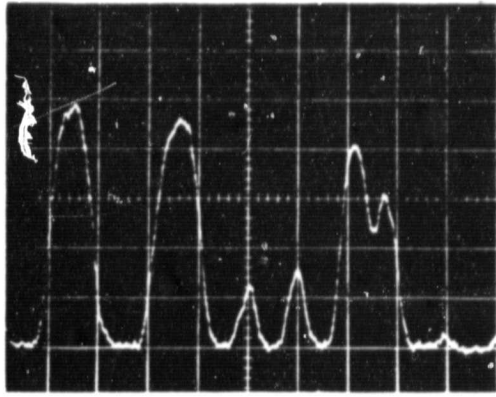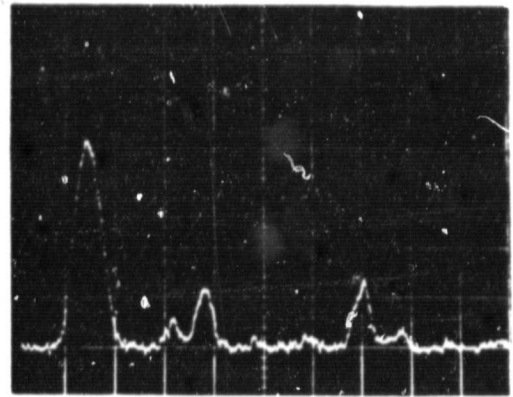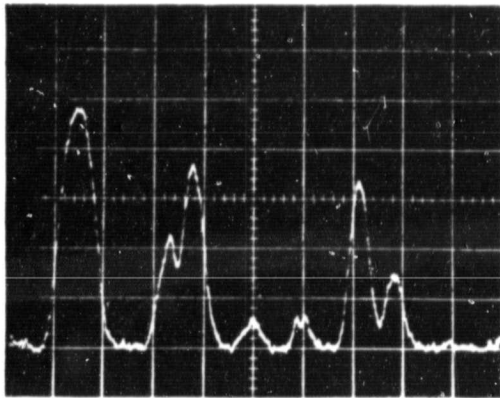
528   Ch #8

528   Ch #11

528   Ch #9
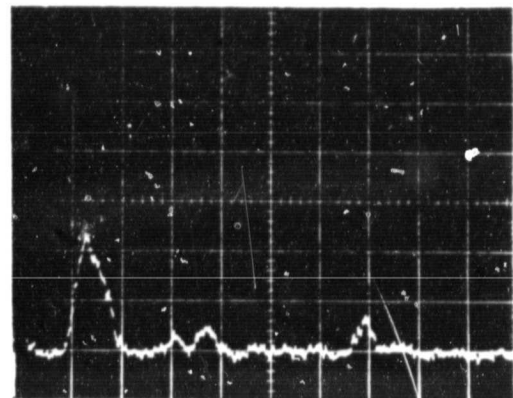
528   Ch #12
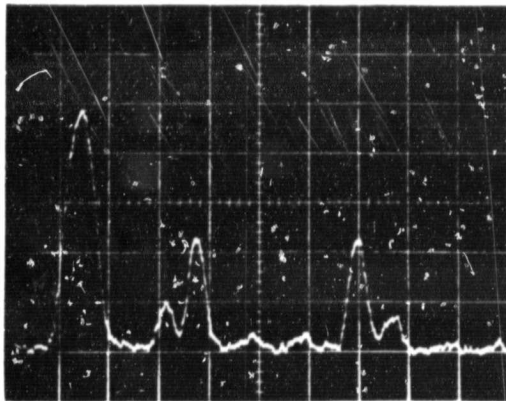
528   Ch #10
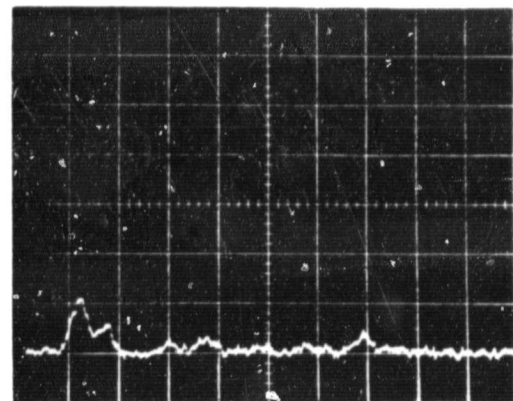
528   Ch #13

Figure 23.   Detector Output for a Nine Blade Spread - Channels 8 Through 13.

40

blade No. 10 in Channel No. 2 with that of blade No. 12 in Channel No. 6, for example, shows that the protrusion difference of these two must be about 4 Channels (76.2 μm or 3 mils). Comparison of blades No. 8 and No. 9 illustrates the interference effect outlined in Sections 4.0 and 5.0. Figures 22 and 23 show that nearly complete attenuation of the radiant energy is produced in Channel No. 3 or No. 4 by blade No. 8, but no evidence of attenuation by blade No. 9 is seen until Channel No. 12 or No. 13, and then the intensity is also probably influenced by blades No. 8 and No. 10. Thus the protrusion difference for No. 8 and No. 9 is about ten channels (190.5 μm or 7.5 mils). As noted in the calculation in Section 5.0 a protrusion difference of 226.1 μm (8.9 mils) is the maximum no-interference difference possible for the angular aperture used, for zero output bundle thickness. This is reduced to 205.7 μm (8.1 mils) for twofold magnification and 185.4 (7.3 mils) for unity magnification if the bundle thickness is included. It is probably reduced a few micrometers more by diffraction effects. Thus blades No. 8 and No. 9 represent about the extreme adjacent-blade difference that this sensor can measure. A still larger difference would lead to no discernable minimum at all related to the shorter blade. Actual engine-mounted rotors are ground so as to very much reduce this characteristic.

Within the limitations of inter-blade interference just discussed, the clearance of each blade can be measured one at a time simply by moving the adjusting screws so that the attenuation of the signal in any given channel, 50% for example, as observed with the oscilloscope, is the same for every blade in turn. The dial indicator is read, for each blade, to determine the distance between the top of the rotor-box end and the hinged top cover carrying the adapter plate. The hinge-pivot to maximum blade protrusion distance is exactly half the hinge-pivot to dial-indicator-pin distance so division of the indicator reading by two gives the clearance for a given blade. As an alternate procedure, not used, the touch probe scale could have been read for each blade, in turn, after the screw adjustment for the correct intensity reduction.

This procedure of observing the response in one channel for each blade was actually carried out. It has the advantage of high sensitivity (clearance can be determined to within 2.5 μm (0.1 mil) or better.) Also there is no error due to digitization. The results are not included here because other experiments described in Section 7.4 showed that the clearance of many blades is significantly changed when the rotor is stopped and then restarted. Another difficulty is that this procedure requires a significant time, of the order of half an hour at least, during which systematic clearance changes can be produced by differential thermal expansion of the rotor and box.

An important result of the d.c. source study was the finding that the clearance range of the blades in this rotor was about 356 μm (14 mils), which exceeds the 254 μm (10 mil) maximum that can be measured with this sensor adjusted for two-fold tip magnification. In order to permit measurement of all the blades in one revolution (i.e. without resetting the adjuster screws), L_2 was changed to give unit magnification, even though the digitization interval was thereby increased to 38.1 μm (1.5 mils).

7.2 VARIATIONS IN BLADE SPACING

Systematic variations in the angular spacing of the blade tips were dis-
covered as a part of an evaluation of the variable period divider. To conduct
this evaluation the adapter plate and optics tube were removed and a pointer
and strobe lamp illuminator were set up as shown in the photo, Figure 24. The
pointer was adjusted so that its tip corresponded to the position of maximum
blade protrusion. The strobe was triggered by amplified BLADE SYNC pulses,
so that the phase angle of the blade and flash could be compared. This study
produced two results. First it was found that the phase delay for any blade
varies slightly with rotor speed. The change appears to be the same at all
angles and is about 11% of one interblade angle (i.e. about 0.45°) for every
1000 rpm change in rotor speed. Modifications in the circuitry have somewhat
reduced this effect but not eliminated it. The effect is too small to detect
except for large changes in rotor speed. The second and more important result
of this study was showing that the blades from No. 1 to No. 20, and especially
from No. 77 to No. 88 have systematically larger angular spacing than the
central group. Again, this is somewhat typical of actual engine rotors due
to wider platformed spacer blades used to make the assembly come out full
using 88 blades. This is illustrated in Figure 25(a) which shows the devi-
ation of the position of each blade from a line having the slope of the
average interblade spacing of the central group. For convenience, the devia-
tion has been expressed as a fraction of the average interblade space. It is
seen from the figure that the deviation of blades in the central group never
exceeds 7% and is usually less than 4%, but it increases for blades near the
loading slot so that for blade No. 86 the deviation exceeds 35%. It is empha-
sized that the difference in spacing of adjacent blades never exceeds 7%, but
almost all the blades above No. 78 (and several below No. 20) have systemat-
ically larger spacing so that there are important cumulative effects. The
consequences of these systematic effects will be discussed in Section 7.3,
following, but it is appropriate to emphasize here that if the large space
blades were randomly positioned among all 88, the systematic effects would
be avoided.

7.3 PULSED-SOURCE OPERATION

7.3.1 Pulsed-Source Driver Scheme

Operation of the sensor in a pulsed-source mode has two advantages.
First, a signal is produced for a well defined interval of the blade motion.
Second, the source current (and hence its radiant intensity) can exceed the
limits for steady-state operation. Since it was simple, we chose to utilize
either the single or 88 equally-spaced pulses generated by the variable period
divider to control a simple source pulse-current generator made up from TR1
and TR2 in the lower right hand part of Figure 33 in Appendix A. Figure 26 is
a block-diagram of the pulsed-source driver scheme. The length of the source
current pulses, 6-1/2 μsec, was a compromise between the detector-amplifier
frequency response (about 3 μsec rise time) and the duty cycle - peak source
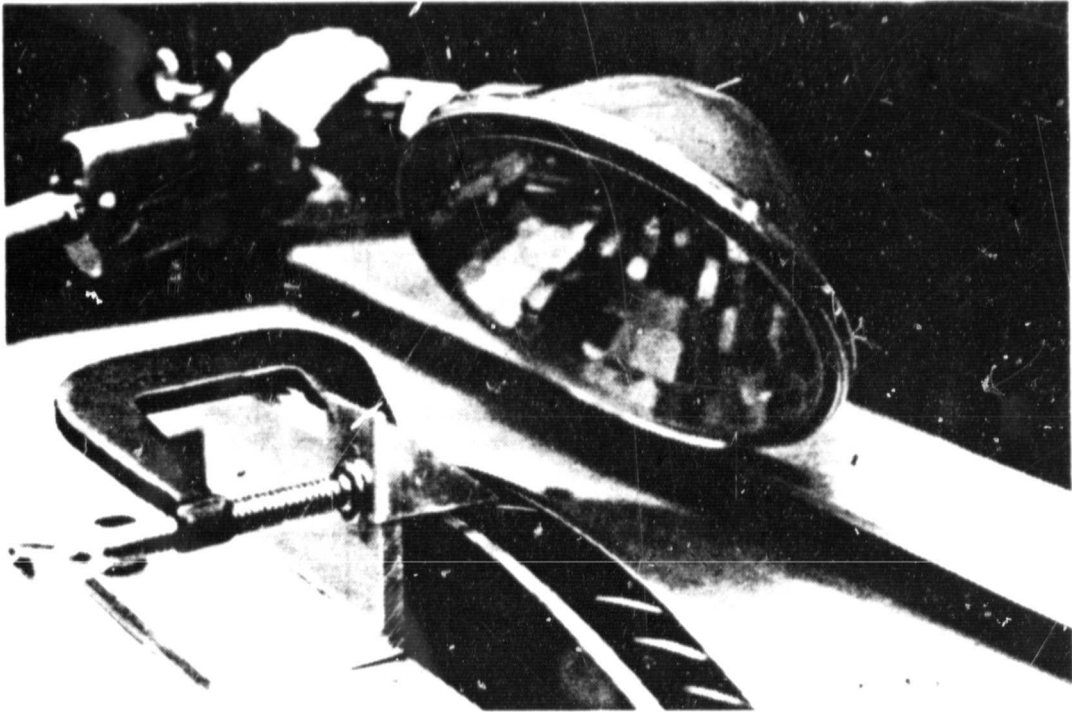
Figure 24. Strobe Light, Pointer, and Top of Rotor With Blades, with Optics Adapter Removed.
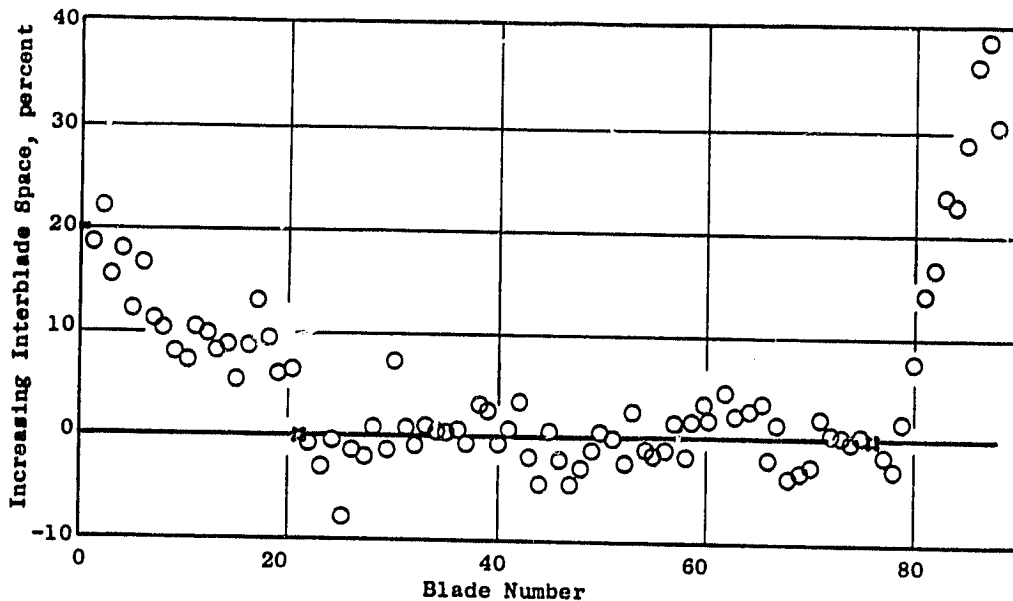
(a) Cumulative Deviation From Constant Blade Spacing (Expressed as Percent of the Average Blade-to-Blade Space Between Blades No. 21 and No. 76.
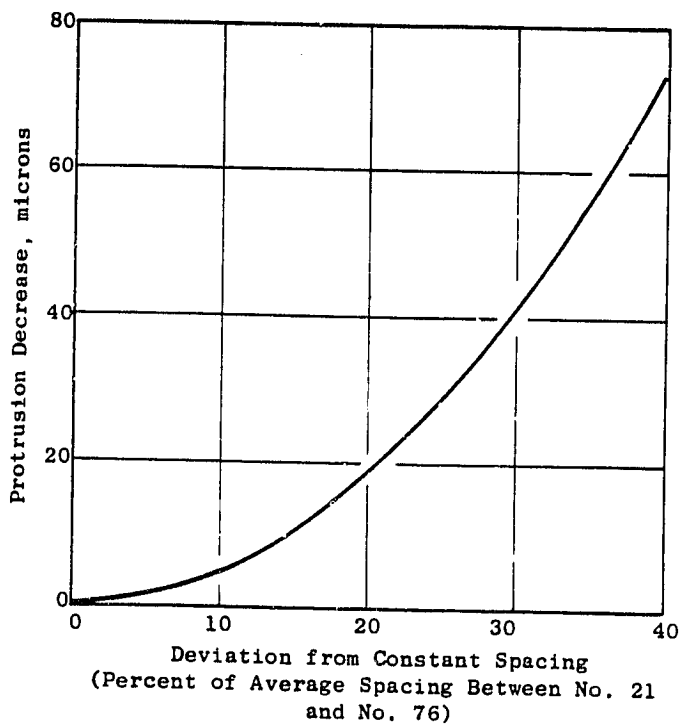
(b) Protrusion Decrease Due to Non-uniform Blade Spacing.

Figure 25. Blade Spacing in the Spin Rig Rotor.

44
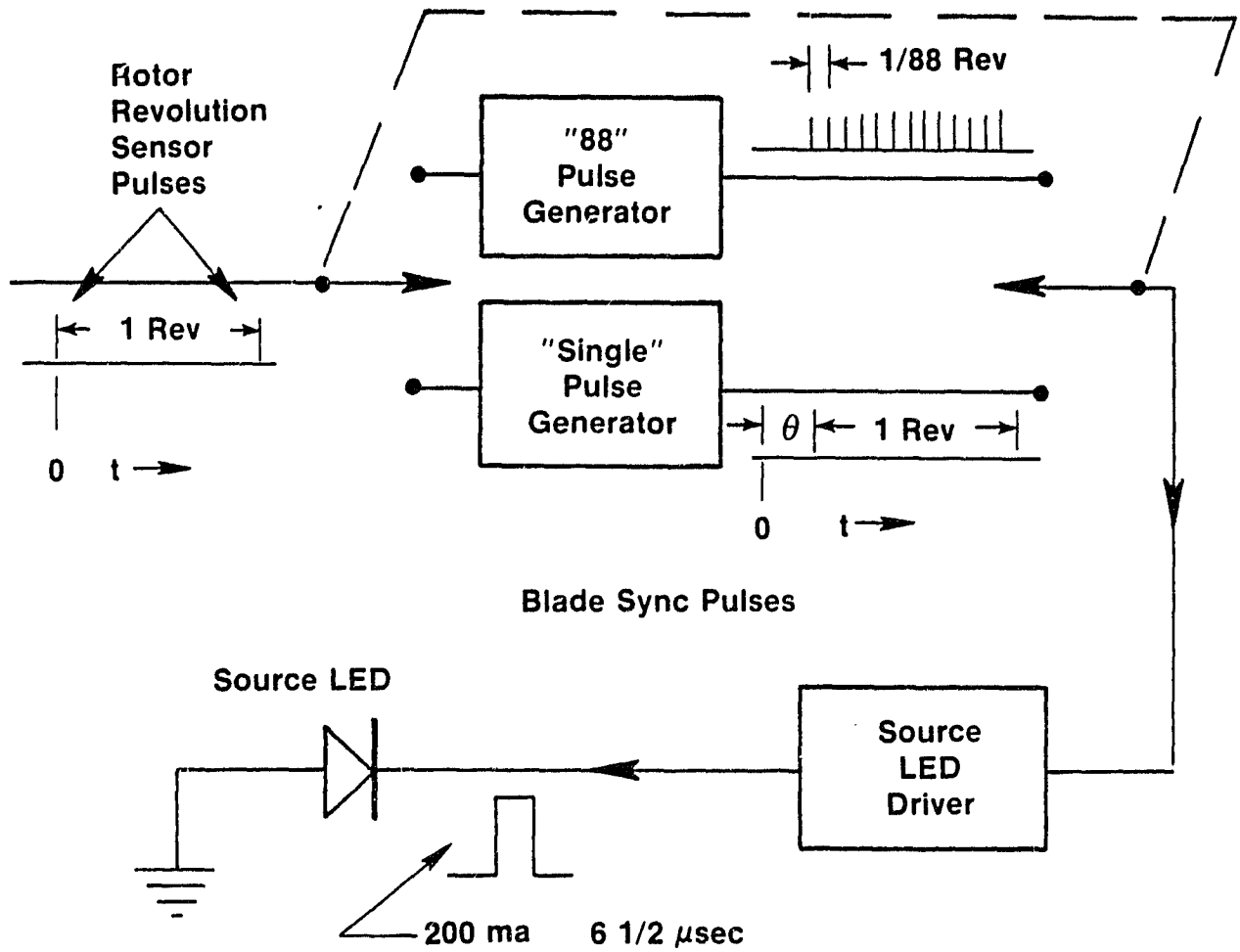
Figure 26. Pulsed-Source Driver Scheme.

current relation (Reference 3) both of which favor a longer source pulse, and the advantage of a pulse short compared to the interblade time ($\approx$40 µsec at 17,000 rpm rotor speed). The optimum choice depends on many factors including the signal processing scheme and electronics, the interblade time, and the source characteristics among others. As already indicated, operation in the single - mode permitted perfect synchronization of one radiant emission pulse per rotor revolution with the instant of maximum protrusion for any one selected blade. However the unequal spacing of the blades [Figure 25(a)] prevents perfect blade-to-pulse synchronization in the 88 mode. The consequences of the imperfect synchronization are indicated in Figure 25(b) which shows the difference between actual blade protrusion and maximum protrusion as a function of the lateral distance between a blade tip and the point of maximum protrusion, for the spin-rig rotor and blades. This figure shows that for lateral deviations less than 10% of the interblade distance, the protrusion difference exceeds 51 µm (2 mils). In our studies the 88-pulse mode was adjusted to give little phase error with the central blade group but consequently there were significant errors in indicated protrusion for blades 83 through 88 with this mode of source operation.

7.3.2 Signal Processing Electronics

Figure 27 is a block diagram of the signal-processing electronics. It is emphasized that the processing scheme, and especially the circuitry, used in this study was designed to take advantage of materials already on hand or quickly and cheaply available, and to suit this particular sensor. It is emphasized that other processing schemes and very different circuits might be needed for a different optical design or for use on an operating engine. Returning to the feasibility study sensor, each of the 15 secondary fiber bundles was coupled to a detector with one of the modules shown in Figure 18. Each bundle was anchored to a module in a way such that reassembly with the same orientation could be made fairly easily if uncoupling was required. The output of each detector was amplified with a three-stage transimpedance amplifier with overall gain of $V_{out} = 4 \times 10^8 I_{in}$ (and about 3 µsec rise time as already noted). A circuit diagram of the amplifier is given in Appendix A (Figure 34). Three LF356 op-amps were used in tandem to secure the required gain and bandwidth; other sensors or op-amps might give adequate performance with only one unit. The source current was adjusted to 200 mA, as measured from the voltage drop in a 1Ω resistor in series with the LED55C source. Under these conditions the amplified detector output was one to two volts depending on the channel observed. The variation between channels is the combined result of infrared transmission variations, bundle-to-detector coupling differences and possibly vignetting effects.

Each three-stage amplifier is followed by an op-amp used as a discriminator, with its output stretched to be about seven times as long as the source LED pulse, i.e. about 40-50 µsec, which is much less than the inter-blade time at the highest spin-rig speed used in our tests (100 µsec). The present component values would have to be modified slightly for operation at 17,000 rpm

46
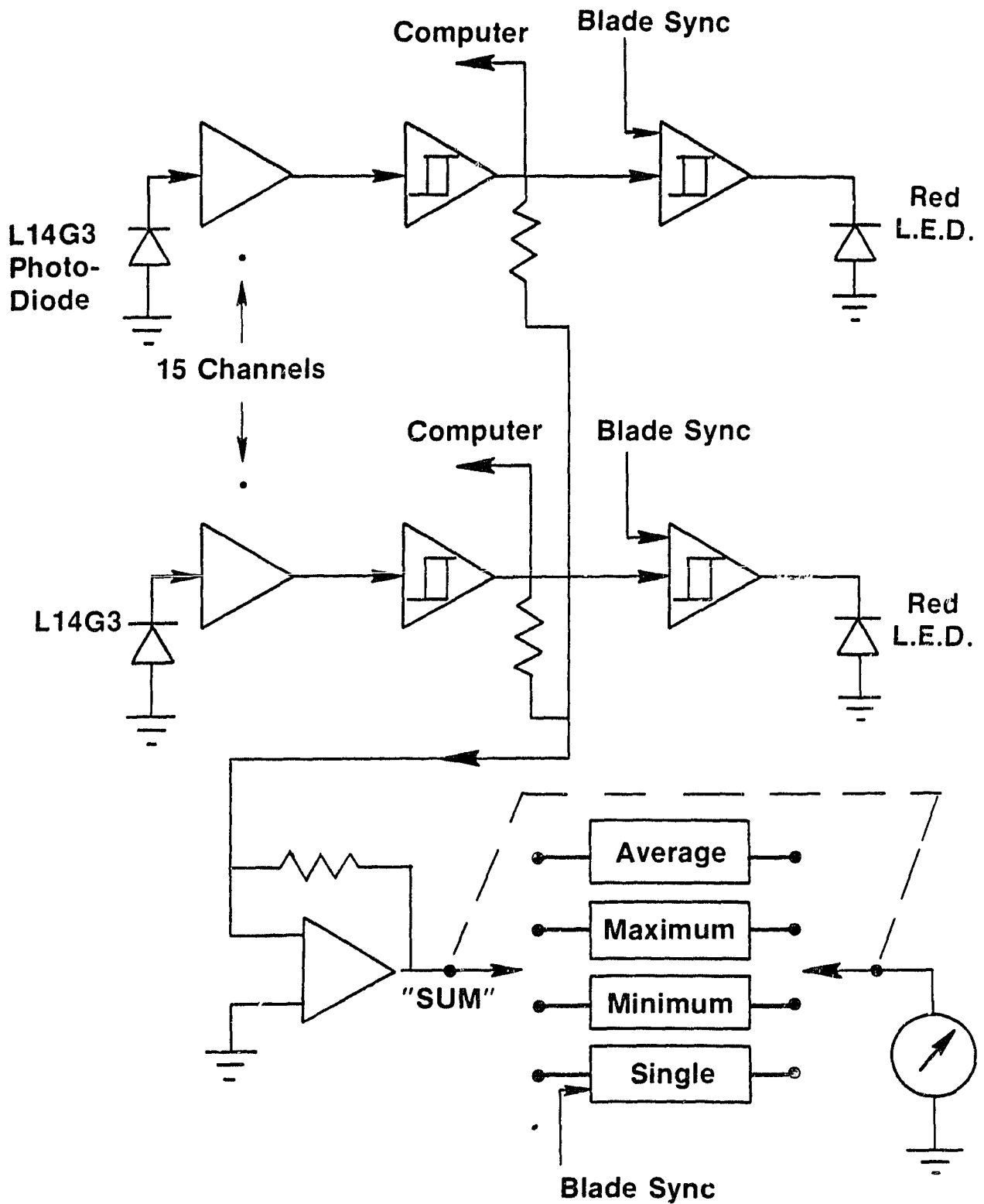
Figure 27. Block Diagram of Signal Processing.

to shorten the stretch to less than the interblade time, 40 μsec. The dis-
crimination level is adjustable with the 10kΩ trim pot, as described in detail
in Appendix A. The discriminators were set to be triggered when a blade height
was midway through a channel width.

Sixteen op-amps are mounted on one circuit board and thus one board can
amplify and discriminate four channels. Four miniature sockets are mounted on
small brackets on each board to connect the bundle-photodetector modules to
the op-amp inputs and to hold the modules to the circuit boards. The four
boards needed for the 15 channels are stacked horizontally with about 2.54 cm
(1 inch) inter-board spacing. Shielding was found necessary between the boards
and is provided by flexible, insulated shields of aluminized mylar.

The 15 discriminator outputs are connected to the drivers for the red in-
dicator LED's to be described below. The connections to the drivers and other
signal processing circuits are through 1 kΩ resistors which, together with the
adjacent capacitors, help isolate the circuitry for each channel. The indica-
tor LED drivers utilize the op-amps in a fifth circuit board mounted about 2.5
cm above the other four. Two of the remaining four op amps in the fourth board
are used as the two-stage amplifier shown in the lower right of Figure 34 in
Appendix A and lower left of Figure 27. This provides the channel-sum output
at S which is connected to the vertical input of an oscilloscope. The sum
output is also used to determine the meter-indicated average, maximum, and
minimum blade clearances as described below. In the 88 mode, 88 source pulses
are provided in each revolution, each pulse occurring at the instant of maxi-
mum protrusion of a blade, within the limitations discussed above and in
Section 7.4, below. Then the oscilloscope connected to S presents a series
of vertical bars (of width equal to the discriminator output pulse width) with
each bar having vertical extent proportional to the number of on-channels for
each source pulse. Thus the bar height is proportional to the blade tip
clearance except for an additive constant which is the same for all blades.

Figure 28 shows an x-y recorder trace obtained by reading out the digi-
tal memory of the oscilloscope. It should be understood that this is essen-
tially equivalent to photographing a single sweep produced by a conventional
oscilloscope. The oscilloscope memory has 4096 channels and is refreshed on
each re-trace of the scope. When used with 10 μsec per channel the time for
one scan across the screen was 41 μsec so that one rotor revolution at
1500 rpm (40 μsec) occupied nearly the full channel capacity of the memory.
At least three channels were employed in storing the sum output for one LED
pulse, and the memory was refreshed every second rotor revolution.

As shown in the signal-processing Block Diagram, Figure 27, and already
mentioned above, the output from each of the discriminators is used to control
a red-emitting LED. This circuitry is described in Appendix A (Figure 35).
These LED's are used only in the single-mode and then indicate if the discrim-
inator for a given channel is on due to radiation received in the channel, for
any given blade. The result is that the number of lit LED's indicate the clear-
ance for the blade selected by the single-mode ten-turn BLADE-SYNC phase-
controlling pot. Comparison of the results thus obtained in the single-mode   ·
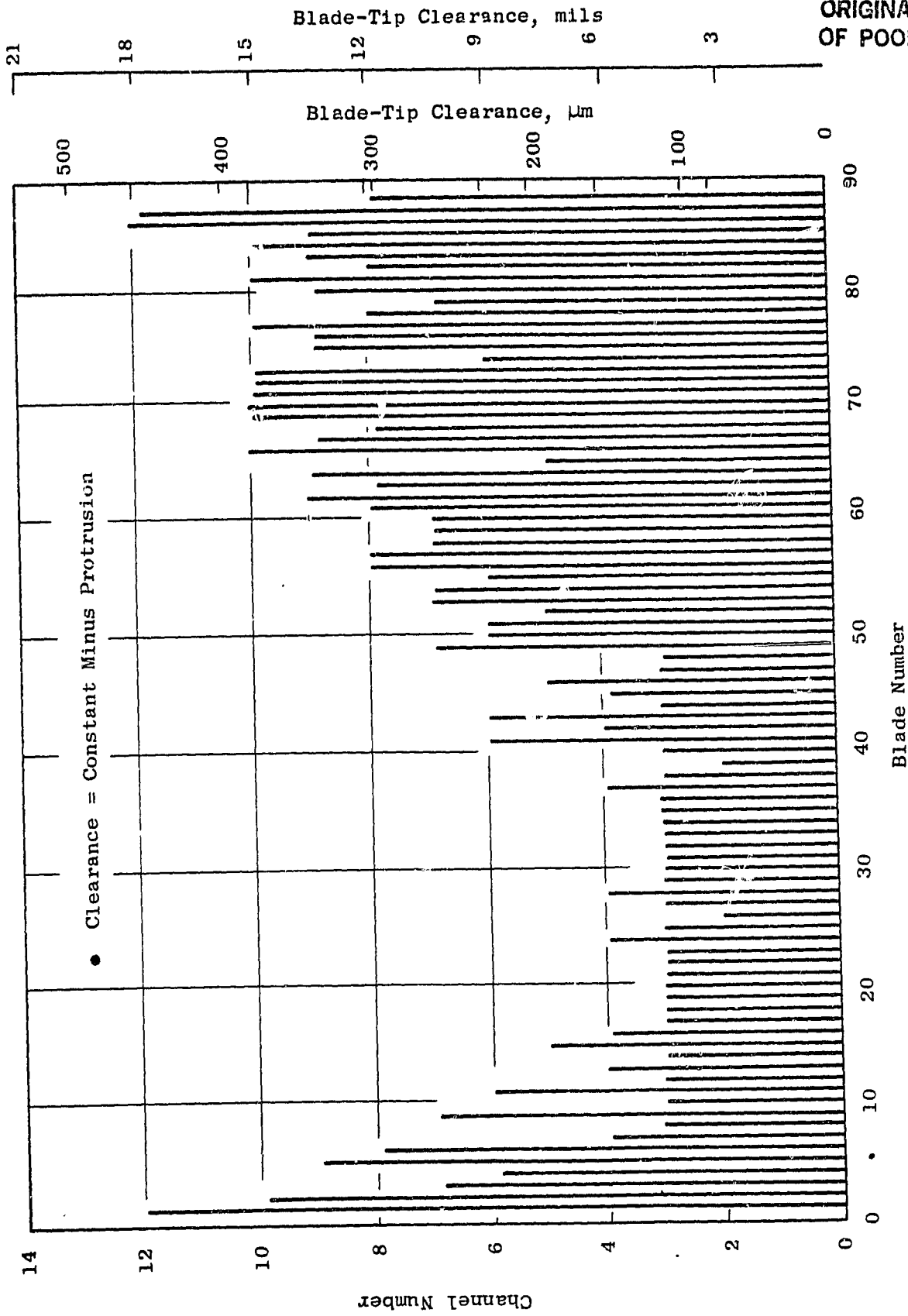
Figure 28. Clearance of Rotor Blade Tips as Measured in One Revolution in the 88-Mode of Source Operation.

49

are useful in verifying the accuracy (or determining the errors) in results obtained in the 88-pulse mode such as the x-y recorder diagram, Figure 28, as well as easily and continuously monitoring the clearance of any specific blade.

Figure 29 is a photograph that shows the 15 red LED's mounted on the top of the rectangular aluminum box that also contains the amplifiers, discriminators, LED drivers, and sum voltage generator. Also shown are a sloping-panel box in the center which controls the BLADE-SYNC pulse generation and timing, and the GaAs source driver-pulse generator, while the sloping-front-panel box on the right produces and selects voltages proportional to the average, maximum and minimum clearance of the 88 blades as measured (once per revolution) in the 88-pulse mode, and also produces a d.c. voltage proportional to the sum output to indicate the clearance of any blade selected in the single-mode. Operation of this circuitry is described in Appendix A (Figure 36).

7.4 VERIFICATION OF THE SENSOR PERFORMANCE AND EFFECTS OF MECHANICAL AND ELECTRICAL NOISE

As already noted, the amplified output from an on-channel (to a discriminator) was found to be 1 to 2 volts (depending on the channel) for a 200 ma source LED current pulse and unit tip magnification, and the RMS noise at the discriminator input for each channel was about 20 mV, so that the peak-to-peak noise was in the 120-150 mV range. Thus the probability of turn-on of a fully off-channel or the turn-off of a fully on-channel was very small and this has in fact never been observed. For a blade that attenuates a channel by a factor of two there is equal probability of its display LED being on or off. What is seen is that the display LED flickers, the flicker being the combined result of the amplifier noise and input-signal noise produced by vibration. The observed decrease in protrusion of a blade required to cause an almost-fully off LED to become almost-fully on is in the range of 5.1 μm (0.2 mils) to 10.2 μm (0.4 mils), except for channel 15 where it is about 20.3 μm (0.8 mils). Channel 15 has a significantly reduced optical transmission for an unknown reason, allowing the same level of noise to have a greater effect.

Figure 30 shows the amplified detector output for Channel No. 7 as the signal was progressively cut off by Blade No. 23 when it was at maximum protrusion. These data were obtained with 200 ma pulsed operation of the driver in the single-mode, with unit tip magnification. It is evident from this curve that when the signal is attenuated by about a factor of two, the peak-to-peak amplifier-output noise (150 mV), is equivalent to about 6.35 μm (0.25 mil) noise in the protrusion. Thus within the accuracy of the measurements the discrimination-uncertainty noted above is fully consistent with the observed electrical noise.

Study of x-y recorder outputs similar to that shown in Figure 28 showed that among five repeated measurements of the 88 blades, the indicated clearance changed by one channel unit (never more than one) for one to nine of the

Figure 29.   Signal Processing and Display Electronics.
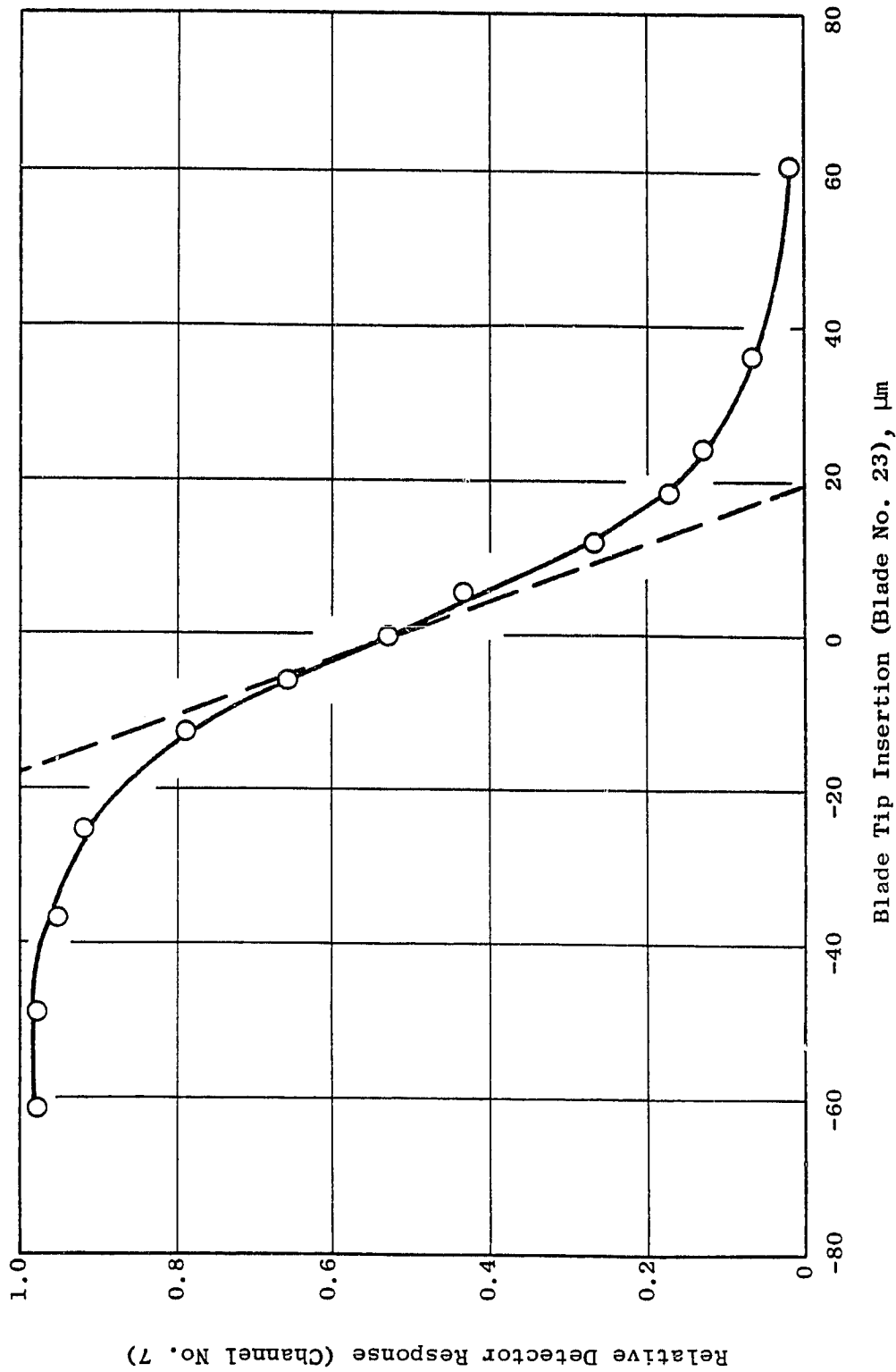
Figure 30. Relative Detector Response as a Function of Blade Protrusion at 1X Magnification.

88 blades (depending on the position of the sensor with the adjustment screws) provided the rotor was not allowed to stop. These changes in the indicated blade length are presumably the combined result of electrical (amplifier) noise and mechanical (vibration) noise. The average number of measurements which change between two successive observations is 3.5. After the five measurements which showed nine values changing, the rotor was started and stopped several times (brought to rest before restarting). Then it was brought to 1500 rpm and the clearance of each blade again measured five times in the 88-blade mode. Comparing the five runs before stopping with the five after, it was found that the number of on-channels had changed by one channel for eleven blades and by two channels for one blade. (In this count we have only included channels where no changes were observed within either of the sets of five runs.) These systematic changes presumably result from real clearance changes that may occur when a rotor is brought to rest.

Comparisons have also been made between clearance measured in the single-mode and in the 88-blade mode. In the single-mode the driver pulse was always set in accord with the true blade position as observed with the strobe lamp and, as already noted, in the 88-mode the driver pulsing was adjusted to obtain the best agreement for the central blade group -- roughly blades No. 10 through No. 80, with poorer agreement resulting for blades No. 1 through No. 8 and especially No. 83 through No. 88. For the central group good agreement was found between 88 and single data, with (infrequent) errors of one channel. However, for the extreme-numbered blades, as defined above, the error was more frequent, and, for blades No. 87 and No. 88, it was two channels rather than one. Also, if it differed at all, the clearance indicated in the 88 mode was always larger than that indicated in the single-mode. All of these differences between the single and 88 mode are consistent with the timing errors related to the systematic changes in blade spacing already discussed. The red LED-display for each blade was also observed (thus with operation in the single-mode) with the rotor spinning at maximum produceable rate, 6000 rpm. No flickering of the LEDs due to mechanical vibration was observed, indicating that these effects were less than about 38.1 μm (1.5 mils). Vibration effects have been observed with the oscilloscope as rapid fluctuations in the signal produced by individual blades at maximum obscuration with DC source operation, but these effects were always equivalent to less than a few micrometers (tenths of a mil) change in tip clearance. These vibration effects did not increase monotonically with rotor speed and affected different blades at different speeds. It is thought that they are related to mechanical resonances in the rotor or blades, or to resonance in the drive system.

8.0 ESTIMATION OF OPERATION IN AN ENGINE ENVIRONMENT

Unless otherwise indicated, the discussion in this section will assume a sensor of the same general type as that explored in this program and with a similar signal generation and processing scheme. Only effects related to source, detector and amplifier temperature will be considered. No attempt will be made to assess possible adverse effects of vibration or of the harsh gas and particle environment inside the engine, since it is thought that these factors, though potentially important, can only be adequately investigated in an actual operating engine.

8.1 ROOM TEMPERATURE PERFORMANCE

Before assessing the performance of the sensor at elevated temperature, its room temperature performance will be considered in the light of the goals of this program. The objective of this program was to demonstrate an optical clearance sensor with a total range of 112 µm (4.4 mils) and an accuracy of 12.7 µm (0.5 mils). Because the rotor in the spin rig showed a maximum variation in blade lengths of about 381 µm (15 mils), it was necessary to use unity magnification and a quantization interval of 38.1 µm (1.5 mils). This quantization of the clearance measurements permits a maximum quantization error of 19.05 µm (0.75 mils). Statistical analysis, assuming a uniform distribution of blade lengths, indicates a theoretical expected rms error, or standard deviation, of $38.1/\sqrt{12} = 11.00$ µm (0.433 mils). Defining accuracy as the standard deviation, σ, this uncertainty is within the goals of the program. This σ is experimentally given by

$$\sigma = \left[\frac{1}{n-1} \sum_{i=1}^{n} (x_i - \bar{x})^2 \right]^{1/2}$$

where σ = standard deviation

  n = number of measurements

  x_i = value of i-th measurements

$$\bar{x} = \frac{1}{n} \sum_{i=1}^{n} x_i = \text{average of all i measurements}$$

If a finer quantization were desired using an output bundle similar to that we have employed, which is apparently the current state-of-the-art, then the signal level would be reduced. At room temperature, reduction could be partially offset by an increase in LED current.

54

The signal at the input to a discriminator was typically 2 volts. The rms noise level at the same point was determined to be typically 20 mV with a voltmeter and about 30 mV by sampling the distribution of noise voltage with the digital oscilloscope. The signal-to-noise ratio, at room temperature and an LED current of 200 mA, was therefore in the range of 60:1 to 100:1.

Electrical or mechanical noise influences the measurement of those blades having lengths such that the signal output in one of the measurement channels is near the discriminator threshold. If there were no noise and the signal were slightly below threshold the discriminator would not trigger. Noise can add to this signal such that triggering occurs, however. Similarly noise can reduce a signal which would be large enough to cause triggering such that it fails to trigger the discriminator.

The range of blade lengths which are influenced by a given noise level depends on the slope of the detector output versus blade insertion, e.g. that shown in Figure 30. From Figure 30, it is seen that a change of 6.35 μm (0.25 mils) changes the signal about 13% or about 0.26V. The peak noise voltage in the electronics used in this feasibility test is about 0.07V so that blades up to about 1.778 μm (0.07 mils) from the threshold point can cause erroneous triggering. In this study, peak voltage is defined as 2.3 times the rms voltage, so that for a Gaussian distribution the absolute value of the instantaneous voltage exceeds the peak voltage about 2% of the time. Thus the maximum error, due to both quantization and noise, is 19.05 + 1.78 = 20.83 μm (0.82 mils). An rms noise voltage of 30 mV corresponds to a blade range of 0.762 μm (0.03 mils), much smaller than the specified accuracy. The total standard deviation expected is $((11.00)^2 + (0.76)^2)^{1/2} = 11.03$ μm (0.434 mils).

One of the objectives of this program is to determine the minimum clearance, or the length of the longest blade. As previously indicated, the quantization of the approach employed is such that even without the influence of noise the determination of the minimum clearance could be in error by 19.05 μm (0.75 mils), with rms error of 11.00 μm (0.433 mils). Noise increases both the maximum and rms errors. For example, is the rms noise was as large as 0.33V, the signal was 2V and the insertion response was that of Figure 30, then the rms uncertainty in blade length introduced by the noise would be 8.38 μm (0.33 mils). Together with the quantization uncertainty the total rms error would be $[(11.00)^2 + (8.38)^2]^{1/2} = 13.83$ μm (0.54 mils), slightly greater than the design goal. If the length of the longest blade is determined as an average over several measurements then the uncertainty introduced by the electrical or mechanical noise is reduced by the square root of the number of measurements. For the preceding example, 4 measurements would give a total standard deviation of 11.771 μm (0.46 mils). Most of this error is due to quantization, not noise.

In monitoring an engine's performance it is also useful to know the average blade clearance. In averaging over all 88 blades the errors due to both quantization and noise tend to partially cancel. More rigorously, the

total error in the sum of the measured lengths of all 88 blades is the square root of the sum of the squares of the errors of all the blades. The average of the blade lengths therefore has an error $1/\sqrt{88}$ as large as a single measurement. With the room temperature signal and noise values this error is 1.255 μm (0.049 mils).

It should be noted that the optoelectronic approach taken requires that the peak noise level is much less than the threshold value (about 1V at room temperatures). If it is not, then the electrical noise can cause erroneous triggering in all of the channels. It may be possible to average over many successive measurements and analyze the results such that the blade length can still be determined when the signal-to-peak noise ratio is of the order of two but we have not evolved an approach as yet.

8.2 PERFORMANCE AT ELEVATED TEMPERATURES

Operation of the source at 120° C reduces the available radiant output from the source LED, and therefore the signal level. Operation of the photodiodes at elevated temperatures reduces their shunt impedance, thus increasing their contribution to the noise level. Operation of the amplifiers and other electronic components at 120° C produces less important performance degradation, provided circuit arrangements are used which are not adversely affected by the changes in DC offset. The GaAs emitter will be considered first. As already noted, the LED55C appears to be electrically identical (and optically quite similar) to the 1N6266, for which extensive data are available concerning pulsed-mode operation. At 17,000 rpm the interblade time is 40 μsec, as already noted, so that 6 μsec LED current pulse length corresponds to a 15% duty cycle. Data (Ref. 4) for the 1N6266 indicate that at 120° C the maximum permissible pulse current is 150 ma. Our data in Figure 8 show that an increase from about 20 to 120° C produces a 3-fold decrease in response for detectors operated in the photovoltaic mode. Thus the maximum permissible 120° source current is equivalent to room-temperature operation at 50 ma. This is a factor of four less than the 200 ma used in our testing. To a reasonably good approximation, the slightly supra-linear emission characteristic and 1.8 fold noise increase (primarily due to the detector) suggest a 33 ma room temperature source operation as reasonably equivalent to 150 ma at 120° C. This is a factor of six smaller than the current used in our tests, but the effect of this reduction can be estimated as follows:

Assuming an LED current of 150 ma and a detector responsivity reduction by a factor of 3, the signal output at 120° C would be reduced by about a factor of four, to about 0.5V. At the same time, the rms noise level would be doubled to about 0.06V rms or about 0.14V peak. With the threshold set to 0.25V the peak noise level is closer to causing erroneous triggering in all channels than is desirable. In principle, however, the system should still function, without improvements, through design changes. An rms noise level of 0.06V, with a signal of 0.5V would produce an rms uncertainty in blade length of 6.096 μm (0.24 mils), according to Figure 30. The rms quantization

56

error is still 11.00 µm (0.43 mils) so the total rms uncertainty in the measurement of one blade with one observation is 12.576 µm (0.50 mils). The maximum error introduced by this noise level is 17.78 µm (0.7 mils). The average clearance could be determined at 120° C to an accuracy of 12.576/$\sqrt{88}$ = 1.341 µm (0.053 mils).

The results, therefore, predict that the basic design used in this feasibility study will function at 120° C. The peak noise level is closer to the value at which the simple processing scheme used here appears to break down, however.

If the signal-processing scheme is not changed, the performance could be improved by increasing the signal at the detector. This could be achieved in several ways. Some of the simpler and more obvious ones are:

1. Increase of the width or length of the row of fibers in a channel or increase in the blade tip magnification. Essentially the signal is proportional to the effective area of a channel (i.e. the true area divided by the magnification). Magnification decrease and width increase would increase the size of the digitization interval. Channel length increase would increase effects related to blade tip irregularities or angle variations.

2. Increase of the optical power emerging from the input bundle into the angular aperture of the sensor. For the short bundles used in this sensor (only a few meters long) the angular distribution of the emergent radiation will resemble that of the source. Thus the high peak radiance of a solid state laser is not offset by its narrow angular range, and especially in pulsed operation such a source might be used to advantage. This is illustrated by the following calculation. The IN6266 is rated at 25 mW/sr at 100 ma, so that 7.5 mW/sr can be expected at 33 ma (at room temperature) and for 6 µsec pulse length, the emitted energy density is 45 x 10^{-9} joule/sr for each pulse. Consider the Laser Diode Laboratories type MH167 GaAs (pulsed) laser. At 70° C it is rated at 35 watts peak power (50 A peak current) from an area 406 µm (16 mils) square with duty factor of 1.6 x 10^{-4}, so that at 17,000 rpm the average total energy for each pulse is 35 x 40 x 10^{-6} x 1.6 x 10^{-4} = 225 x 10^{-9} joule in a beam 24 degrees in width (at 50% intensity). As a rough estimate, this angular width corresponds to about 0.15 sr solid angle so the laser energy density is roughly 1500 x 10^{-9} j/sr. Assuming the LED can produce 100 x 10^{-9} j/sr at 70° C, and recognizing that the laser might need to be magnified by a factor of about 3-1/2 to optimally couple it to the input fiber bundle of 1.588 mm (1/16 inch) diameter, the optical power emerging in a small central solid angle should be comparable for the two sources. The laser has the drawbacks that cooling is essential (to 70° C) and the life at

70° C under the specified conditions is not known. It is worth noting also that cooling the LED to room temperature (25° C) would permit a current increase to 650 ma and this should result in performance better than that actually achieved at 200 ma at room temperature.

3. LEDs have been recently introduced which have a higher radiance than the types considered in this study. These may be useful in an optical clearance sensor.

In addition to increasing the signal level it may be possible to find photodetector/pre-amplifier combinations having a lower noise level.

9.0 ASSESSMENT OF SENSOR CONCEPT POTENTIAL

9.1 AIRCRAFT ENGINE APPLICATIONS

9.1.1 Efficiency Monitor

Efficiency loss due to airfoil tip clearances at any given engine rotor stage is related to the circumferential average clearance of all the blades in that stage. The sensor concept investigated in this study has the possibility of determining this average at any one circumferential position for each sensor mounted. The complexity of the sensing system, including number of channels required, depends on the system under consideration and the characteristics of the rotor being monitored. For example, the blade tip clearance range must be less than the measurement range of the sensor if the average clearance is to be determined. The sensor discussed in our feasibility study divides the tip clearance range into fifteen radial digitization intervals (output fiber optic bundle layer channels), and the average clearance is determined from the sum of the clearances for the individual blades for one revolution. As was described in Section 8, the average clearance can be determined at room temperature or 120° C to 1.27 μm (0.05 mils) with quantization employed. This accuracy should be adequate for any efficiency monitoring application.

It is certain that the TF34 stage nine compressor disk and blade assembly in our study did not contain blade-to-blade height variations realistic of typical engine hardware. The blades assembled were a mixture of used blades from more than one engine teardown and several new blades. In an actual engine rotor, each stage is accurately ground to a specific diameter. Thus the sensor aperture width could generally be increased from that used in the feasibility study, as discussed in Section 5.2, allowing transmission of more radiant energy and increased sensor accuracy. A calculation of the accuracy of the average measurement in relation to sensor and rotor parameters is possible.

The feasibility study sensor was designed with eventual adaption to the TF34 stage nine compressor in mind, where cold tip clearance is nominally set around 0.813 millimeters (32 mils). From this maximum clearance to the zero clearance condition could be measured with suitable optical design. The NASA Energy Efficient Engine is slated for use of active tip clearance control on the compressor and both turbines. E^3 compressor tip clearances range up to about 0.635 millimeters (25 mils). Several sensors would probably be necessary to get a circumferential mapping.

9.1.2 Control System Sensor

The requirements for a control system may be quite different from those of an efficiency monitor. A limited number of sensor channels could indicate approximate regions of clearance to help determine compressor cooling air

valve switch points on such engines as the E^3. For instance, when cruising at altitude and with 5th stage air cooling the casing stages six through ten to lessen clearances for efficiency, a clearance measurement could allow a minimum clearance to be reached safely. A single sensor channel might indicate when the clearance reaches a predetermined minimum value.

A control system sensor need measure only maximum blade height protrusion. This blade could be predetermined from cold clearance static calibrations, and in our single blade sensor mode, the light pulse delay could be set manually to trigger on that particular blade at any speed. This blade alone could then be monitored over whatever range is needed. A single sensor with a strategic circumferential position based on test cell data using multiple sensors, should be sufficient. Sensor signal processing of this application would be considerably simpler than that developed in our experiments.

9.2 SENSOR CONCEPT VARIATION WITHOUT A TIMING PULSE

The sensor developed in our feasibility study required a relatively precise timing pulse once in each revolution of the rotor at a known circumferential position with respect to the rotor blades. The usual engine core speed electrical signal is a sinusoidal waveform from the control alternator which is driven by a fuel pump mounted to the gearbox. If this signal does not provide the timing precision required for the sensor, a dedicated sensor may need to be devised, or a different mode of sensor operation developed that does not require a timing pulse. For example, with a continuous source (DC operation) the minimum clearance would be indicated by the extreme channel obscured over a period of at least one revolution. With a non-quantized system the minimum clearance is indicated by the minimum transmission. Either of these extreme values can be determined without regard to the absolute angular position of the rotor. Similarly, the efficiency can be monitored through the average channel obscuration, or average DC transmission. Because the radiant transmission increases during the time intervals when no blade is normal to the optical axis (at the position of maximum obscuration) the average transmission would be higher than that determined only when the blades fully intersect the optical path. The error introduced by this offset has not been analyzed. If it is too great, it may be possible to devise a signal processing approach which samples the transmission (in either a quantized or analog optical system) and determine the minimum value as each blade intersects the sensor beam, without reference to a synchronizing pulse. Determination of the feasibility of this approach would require further study and electronics development and was not included in the scope of this program.

9.3 MORE COMPACT SENSOR DESIGNS

Mounting space for components on aircraft engines is at a premium. The dimensions and configuration of the feasibility study sensor were selected to utilize readily available lenses and relatively simple construction. Being

60

tangential to the rotor, the sensor has an inherent wrap-around nature which could be advantageous in certain tight envelope situations and where engine structure prevents direct radial insertion. However, more compact designs are possible, either in a circumferential or radial mounting profile.

Figure 31 depicts an approach using mirrors which may be applicable to single hole mounting. A critical dimensional consideration is the clearance between the moving blades and the output mirror. The discussions in Section 5.0 of this report can be applied to calculate the mirror size for a specific bladed rotor, as well as other design details which are less important from a feasibility standpoint such as fiber bundle sizes, lens diameters and angular aperture.

Figure 32 is an approach where the objective was to minimize the enlargement of the gap introduced by the sensor itself. The input and output bundles occupy two separate radial holes. The access holes would be sealed by windows, perhaps fabricated from sapphire or some other abrasion-resistant material. For typical angular apertures and a clearance range of about 250 μm (10 mils), the illuminated portion of the windows would be about 17.8 mm (0.7 inch) in the circumferential direction. The approach also incorporates prisms which internally reflect the optical beam such that it enters and leaves the engine in a radial direction.
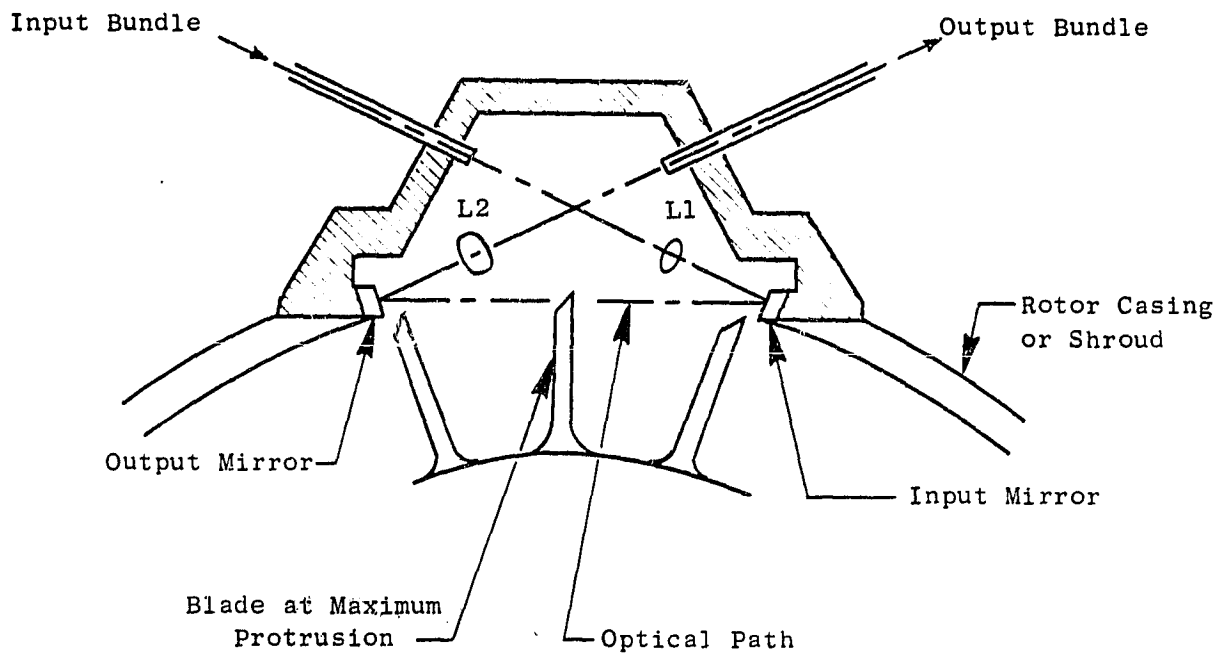
Figure 31. Compact Sensor Approach Using Mirrors.
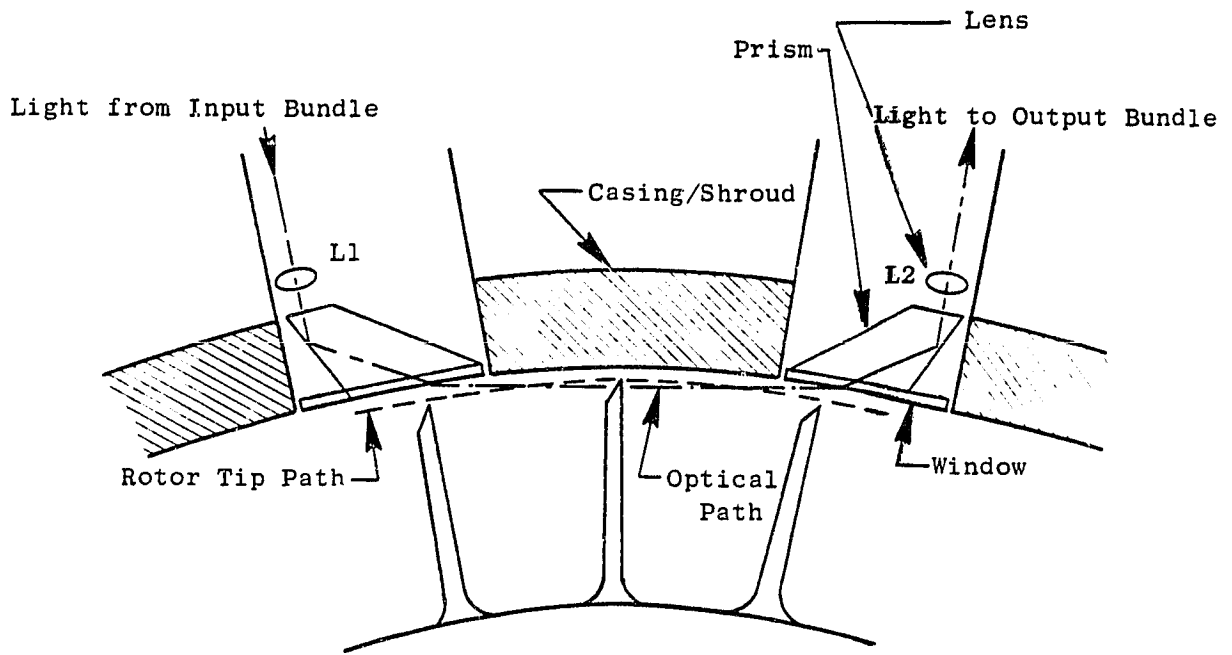
Figure 32. Compact Sensor Approach Using Prisms.

10.0 DISCUSSION OF RESULTS

10.1 COMPONENT EVALUATION

Elevated-temperature performance tests were carried out on several optical and electronic components of the optical tip clearance sensor. The tests included determination of the integrity and transmission of an optical fiber bundle, decrease in signal from GaAs LED source/Si photodiode combinations, decrease in shunt resistance in certain Si photodiodes, and noise increase and d.c. output offset change in operational amplifiers. The results encouraged proceeding into the design and testing phase of the optical tip clearance sensor concept.

10.2 SENSOR DESIGN AND TESTING AT ROOM TEMPERATURE

General design principles pertaining to the sensor concept relating to rotor geometry, optical component dimensions, and diffraction limitations have been described. The result is a design base which can be used in applying the sensor to any particular rotor configuration.

The general principles developed were applied to the design of a sensor to study the feasibility of our optical tip clearance sensor concept at room temperature. No attempt was made to minimize sensor size. The feasibility sensor was mounted to a test rig which included a TF34 stage nine compressor disk and blades. Using d.c. source operation and a selected blade trigger pulse, the compressor rotor was studied, producing a measure of each blade's relative height and general rotor eccentricity. Using a pulsed-source mode of operation, the radiant intensity was increased and all 88 blade heights were measured in any chosen rotor revolution. Errors due to nonuniform blade spacing were discussed. Using the output layerwise coherent optic cable, which has a maximum quantization error at unit magnification of 19.05 μm (0.75 mils), statistical analysis showed that on an rms or standard deviation basis, the quantization plus noise error is around 11.03 μm (0.43 mils), less than the 12.7 μm (0.5 mil) design objective. In addition, using multiple measurements of the single tallest blade (minimum clearance sensor) or averaging over all 88 blades, further reduces the expected error.

10.3 ESTIMATION OF PERFORMANCE AT ELEVATED TEMPERATURES

Operation of the source, photodiodes, and amplifiers at elevated temperatures reduces the signal to noise ratio levels significantly, although the basic design will function. Peak noise levels are almost intolerable in our simple processing scheme. Several methods have been given by which the performance could be improved by increasing the signal at the detector. Also, it may be possible to find photodetector/preamplifier combinations having a lower noise level.

64

10.4 RECOMMENDATIONS FOR FUTURE WORK

Due to the results of the feasibility study sensor testing, it is believed that this optical tip clearance sensor should be developed into an aircraft engine prototype sensor. The initial task should be choice of a particular vehicle and mounting location with a clearly defined applicational purpose and well-defined performance requirements. A detailed design can proceed after such things as rotor size and speed, measurement range and purpose, engine operating conditions including temperature, vibration, and corrosion, and physical size constraints are known.

Although specific sensor designs depend strongly on the purpose and detailed requirements, several factors needing further study are common to all designs. These studies could be performed concurrent with the detail design work mentioned above, after an engine application is chosen. They include:

1. Mechanical integrity and optical performance of incoherent and layer-wise coherent fiber bundles under combined engine environment such as temperature and vibration. This may require on-engine testing.

2. Performance of lenses, mirrors, and optical windows under engine operating conditions of temperature, abrasion by gas-borne particles, and attack by corrosive atmospheres.

3. Study of sensor modes of operation which do not require rotor generated triggering pulses related to rotor phase angle. Blade spacing irregularities would have much less affect.

10.5 CONCLUSIONS

It has been demonstrated through testing that the optical tip clearance sensor concept studied in this program is capable of measuring blade tip clearance to a significant degree of accuracy at room temperature. Performance predictions based on the test results from those sensor components tested at engine operating temperatures, agree with this conclusion, although to maintain the same level of accuracy, signal processing modifications to the studied concept may have to be made. Also, more compact configurations of the sensor concept have been depicted. Therefore, it would be worthwhile to proceed into a design program to develop this sensor concept into an aircraft engine prototype sensor for on-engine testing.

APPENDIX A

CIRCUIT DIAGRAMS

Figure 33 is a circuit diagram of the variable period divider. It operates as follows: The once-per-revolution pulses from the magnetic sensor are first shaped and amplified, and then control the generation of all other pulses. Immediately following this initial pulse a second pulse is generated which resets a linear ramping circuit. (To increase the accuracy over a wide range of rotation rates, the current feeding the ramp generator is made proportional to the rotor rotation rate.) The initial pulse controls a sample-and-hold circuit to sample the peak value of the ramp. In the single-mode this peak value is divided with a highly linear ten-turn pot with front panel control. The resulting signal is fed into a comparator circuit that triggers when the ramping voltage equals the pot-selected voltage. In a second mode of operation, the 88-mode, 88 equally spaced pulses are generated in each revolution, but as before the pulses are equally spaced in phase independent of rotor speed. In this mode the phase of the first pulse and the phase-spacing of the 88 pulses are adjustable. Z4B output pins 9 and 10 are synchronous pulses about 6 μsec in duration. These pulse outputs occur either once per revolution or 88 times per revolution depending on whether the output at OP6 or OP9 is selected by the front panel switch marked "single" or "88". The pulse from pin 9 of Z4B is stretched by Z4A to be 31 μsec long, starting synchronous with that from pin 10. The stretched output from pin 6 of Z4A is THE BLADE-SYNC output used to trigger the oscilloscope in the DC-source studies while the unstretched output from pin 10 of Z4B is used to control the generation of current pulses (by TR1 and TR2) to drive the LED55C in the pulsed-mode source studies described in Section 7.3.

Figure 34 is a circuit diagram of the three-stage trans-impedance amplifier for the output of each channel detector. The op-amp discriminator trigger levels were set as follows: The D.C. offset of the second and third amplifier op-amps was adjusted to zero for all 15 channels. Then the discrimination threshold of the top channel No. 1 was adjusted so that it occurred at 100 ma source LED current (half of the usual 200 ma). Next, with the source LED pulsed at 50 Hz and 200 ma by triggering from a signal generator rather than the magnetic pickup and with the rotor stationary but oriented so that the tallest blade was in the sharp focus position, the whole sensor was lowered with the adjuster screws until the signal output of the No. 1 detector was attenuated by a factor of two as evidenced by the discriminator response. The dial indicator showing the distance between the end of the hinged top and the top of the box housing the rotor was set to read zero. The adjustor screws were now moved (together) so as to lower the end of the hinged top by 76.2 μm (3 mils) [i.e., lowering the sensor by 38.1 μm (1.5 mils), the width of a fiber row in the output bundle]. The discriminator for channel No. 2 was adjusted to the triggering threshold value. This procedure was repeated

Figure 33. Variable Period Divider.

68

Figure 34.   Fifteen Channel Preamp, Trigger, and Summing Circuitry.

for each channel in turn, through 15. A check showed that the threshold so established in channel 15 also accurately corresponded to that produced by a twofold LED current reduction

Figure 35 includes a diagram of the red LED-display/microprocessor drivers. Referring to this figure, the circuitry and op-amp directly connected to BLADE-SYNC generates the waveform shown. The signal at the non-inverting op-amp input rises within a fraction of a microsecond when the BLADE SYNC pulse starts, and then gradually falls, while the signal at the inverting input rises relatively slowly to the full BLADE SYNC pulse height. The result is that a sharp (negative) pulse is generated just as the BLADE SYNC pulse starts, followed by a rise to a positive value within a few microseconds and a fall to zero when the BLADE SYNC pulse ends. This waveform is applied to the inverting input of the 15 display LED-driver op amps. Initially the driver op amp output is positive (at about four volts) and the LED (D2) is not lit. The positive feedback (through the 47k resistor and capacitor) maintains the positive output so long as pin 2 of the op-amp is at a more negative potential than pin 3. The values of the resistors are selected so that this does not occur unless both a pulse from a discriminator enters at P1....P15 and the positive-going component of the modified BLADE SYNC pulse occurs. If this does occur, pin 2 of a driver op-amp does become more positive than pin 3, the output from pin 6 goes negative (at about minus four volts), D2 conducts, and (red) light is emitted. This condition is maintained (pin 2 more positive than pin 3) until the negative-going pulse from the modified BLADE SYNC arrives at pin 2 of the drivers. Since pin 3 is then more positive than pin 2 the driver op-amp output returns to the positive state and the display LED goes out. Thus a red LED turns on only if the discriminator for that channel produces a pulse (due to radiant energy arriving at the corresponding detector coupled to the fiber bundle) and it stays on essentially the whole rotor revolution (in the single-mode) until it is turned off by the start of the next BLADE SYNC pulse.

The circuit at the bottom of Figure 36, the SIGNAL-PROCESSOR schematic, generates the pulse S' from S. S' is the input for all the processing circuits in this diagram. S' is generated by the switching of S by Z2B which is activated by the DATA SYNC pulse. DATA SYNC is generated from BLADE-SYNC by Z3A and Z3B. It starts after BLADE-SYNC (with delay controlled by Z3A) and ends after about 20 μsec, (as controlled by Z3B). Thus S' (pins 4 and 16 of Z2B) is a sample of S that starts after all the discriminators have been activated and ends before any have returned to their initial states. Hence S' is not affected by variations of hold time among the 15 discriminators.

Routing of S' to the average, single, or max/min circuits is selected by positions 1, 2, or 3 of switch B, while the outputs from these circuits are fed to the meter-driver circuit by positions 1, 2, or 3 of switch A. The average circuit is used only in the 88-pulse source mode. It is simply an integrator which is reset once per rotor revolution when the (short) RESET pulse is applied to Z1A. The integrator output is at pin 1 of T_{11}. The single-circuit is used only in the single-pulse source mode. It is a sample-and-hold circuit. The input capacitor (0.01 mfd mylar) is charged to the voltage (from an op-amp) that generates S's, so that the output (pin 2 of

70
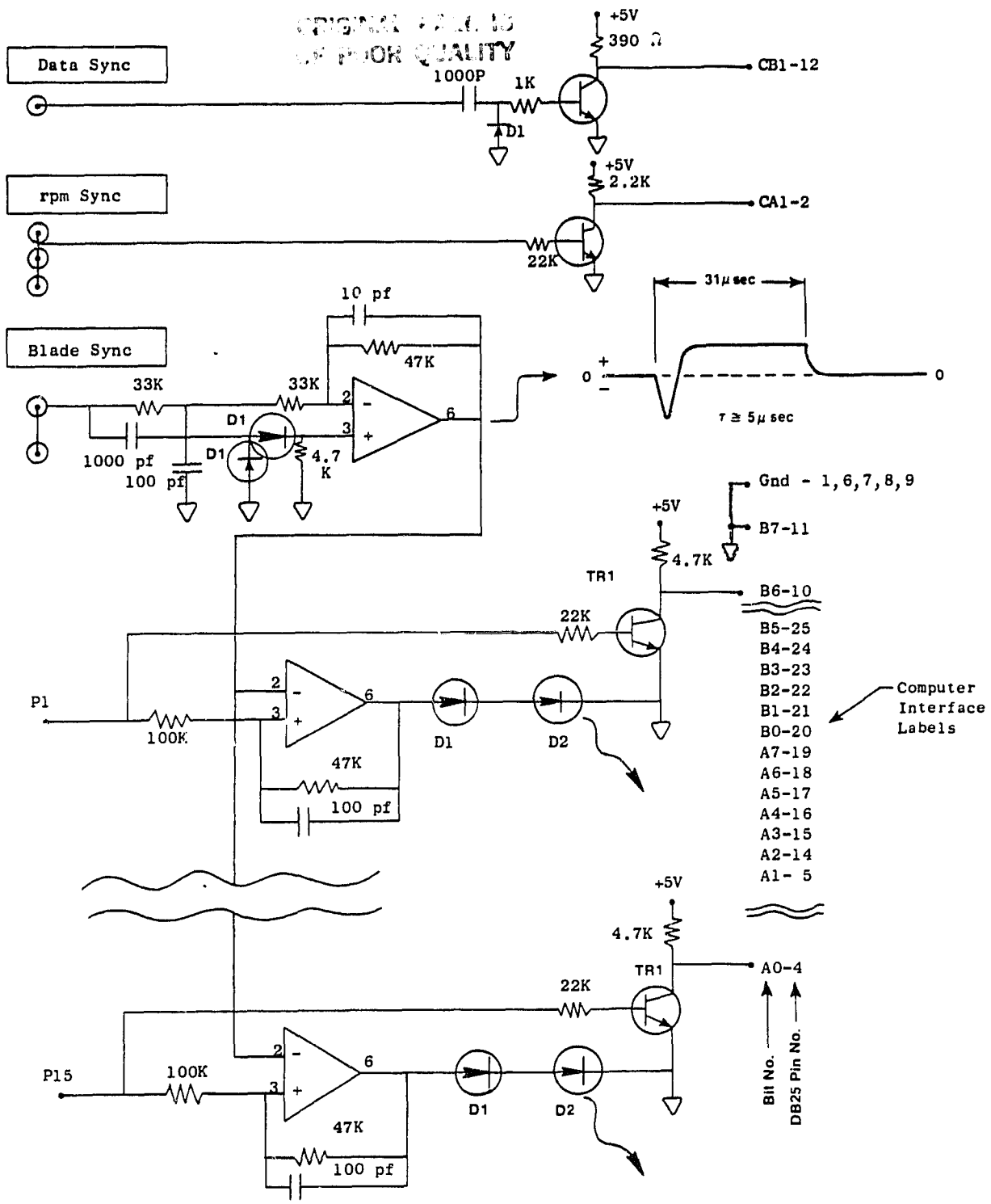
Figure 35. LED Display/Microprocessor Drivers.
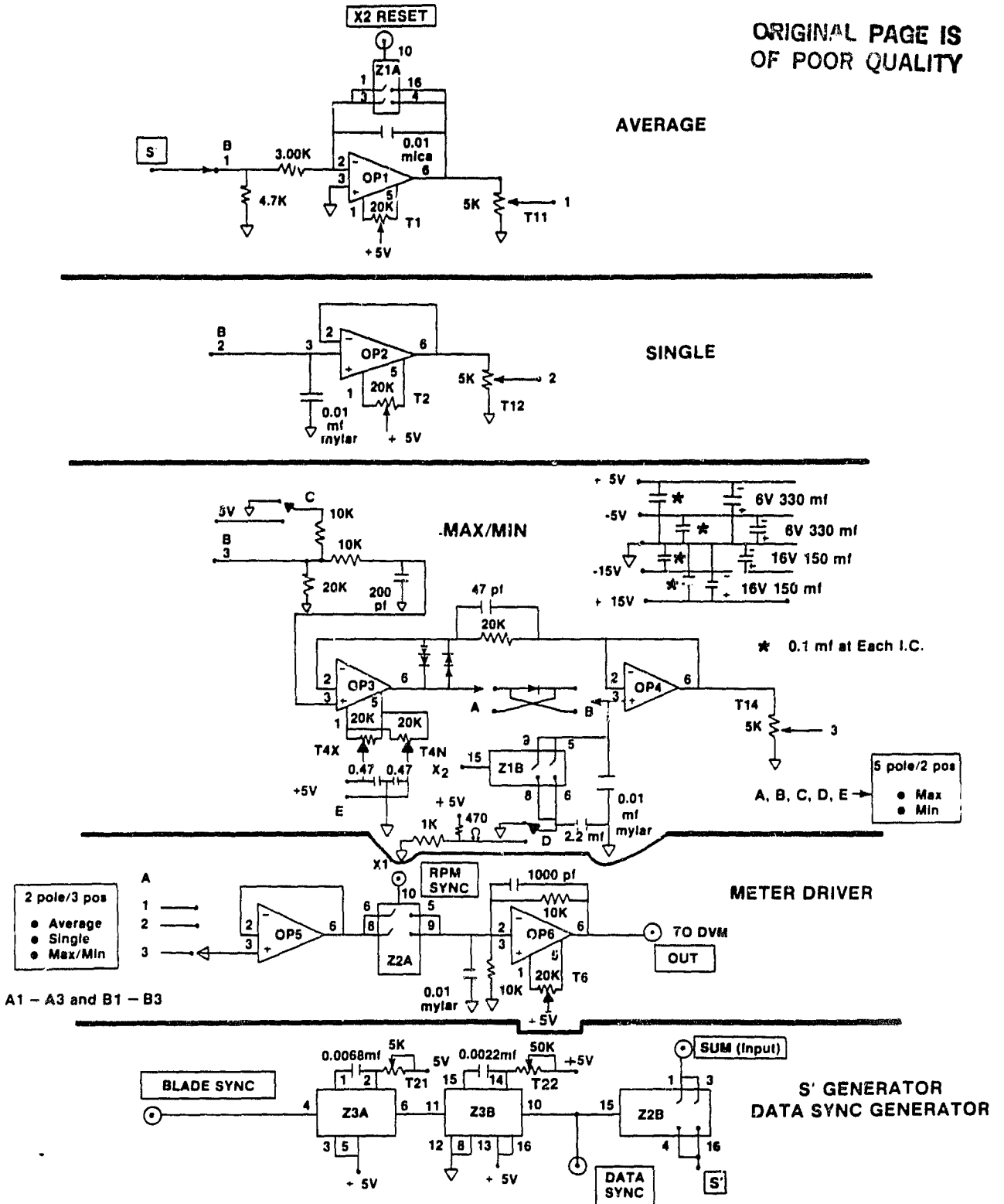
Figure 36. Signal Processor Analog Display.

T_{12}) is proportional to the sum signal S' for the blade selected by the source when it is activated by a pulse synchronous with BLADE-SYNC, once per revolution. The max/min circuit operates only in the 88-pulse source mode. It uses the diode connected between points A and B (between OP3 and OP4) to select either the largest or the smallest of the 88 S' pulses in one revolution to activate the sample-and-hold circuit OP4 which is reset every revolution by Z1B when this in turn is activated by RESET. The sample-and-hold output (i.e. max or min) appears at pin 3 of T_{14}.

The meter driver (drawn just above the S' generator near the bottom of the schematic) consists of a buffer amplifier OP5 that accepts the output from one of the three circuits above. The OP5 output is sampled once each revolution by Z2A and held (for one revolution) by OP6, the output of which is read on a digital voltmeter. All the circuits are calibrated (using T_{11}, T_{12}, and T_{14}) so that the absolute value of the meter-driver output in millivolts, is numerically equal to the clearance in mils, with zero in all cases taken as full obstruction of all fifteen channels.

REFERENCES

1. Jenkins and White, 2nd Edition, pp. 282-292

2. Born and Wolf, 5th Edition, pp. 393-395 and Figure 8.9.

3. GE Optoelectronics Manual, copyright 1979, Syracuse, N.Y., p. 106 (IN6266).